

ABSTRACT

MAHBOOBA, ZAYNAB MUNTHER. Electron Beam Melt Fabricated Ti6Al4V with Boron Additions: A First Step Towards Tailoring Composition and Microstructure for Additive Manufacturing (Under the direction of Dr. Ola Harrysson and Dr. Srikanth Pathala).

Additive manufacturing is a technology used to fabricate three-dimensional parts from computer models by consolidating materials layer-by-layer. Additive manufacturing offers advantages in design flexibility and material efficiency and is often used to produce Ti6Al4V for the aerospace and medical industries. Electron beam melting (EBM) is an additive manufacturing powder bed fusion process in which metal powders are selectively melted by an electron beam. The morphology of EBM built parts is unique; specifically, Ti6Al4V fabricated with EBM exhibits an inhomogeneous and columnar microstructure. While anisotropy is desirable for certain applications, in others a more isotropic and refined structure may be required. It is possible to control microstructure by altering processing parameters in additive manufacturing; however, the window for parameter variation for some materials is very small, and alternative methods must be employed to customize microstructures. Hypoeutectic additions of boron have proven to refine grain size, increase strength and decrease ductility in Ti6Al4V castings. It is likely that this mechanism will take place in EBM fabricated Ti6Al4V and produce more refined, equiaxed microstructures while increasing strength. A systematic study was conducted using Ti6Al4V powder with pre-alloyed and blended additions of boron ranging from 0.1 to 1.0 weight fractions. Samples were built using the Ti6Al4V parameter set in the Arcam EBM machine, and were characterized using optical microscopy, electron backscatter diffraction, x-ray diffraction, inductively coupled plasma mass spectrometry, combustion analysis, microhardness, flexural testing and tensile testing. Preliminary work suggests that a unique grain refinement

mechanism might be taking place in EBM fabricated Ti6Al4V+B, and that there is an opportunity for mechanical property improvement. This work highlights the growing need to tailor alloy chemistry to suit the unique requirements of additive manufacturing.

© Copyright 2015 by Zaynab Munther Mahbooba

All Rights Reserved

Electron Beam Melt Fabricated Ti6Al4V with Boron Additions: A First Step Towards
Tailoring Composition and Microstructure for Additive Manufacturing

by
Zaynab Munther Mahbooba

A thesis submitted to the Graduate Faculty of
North Carolina State University
in partial fulfillment of the
requirements for the degree of
Master of Science

Materials Science and Engineering

Raleigh, North Carolina
2015

APPROVED BY:

Dr. Ola Harrysson
Committee Co-Chair

Dr. Srikanth Patala
Committee Co-Chair

Dr. Harvey West

Dr. Timothy Horn

Dr. Ronald Scattergood

BIOGRAPHY

Zaynab Mahbooba was born and raised in Raleigh, North Carolina. She received her B.S. from the department of Materials Science and Engineering at North Carolina State University in 2013.

ACKNOWLEDGMENTS

Firstly, I want to express my appreciation to Dr. Ola Harrysson, Dr. Harvey West, Dr. Timothy Horn, Dr. Srikanth Patala and Dr. Ronald Scattergood for their involvement in my graduate committee. Additionally, I was to thank Dr. Ola Harrysson for funding this project and for his advisement and patience for the last two years. I want to graciously thank Dr. Timothy Horn for inspiring the topic of this project and for his guidance throughout this research. I am grateful to Dr. Harvey West for providing his expertise on breaking stuff and for his sharing his knowledge of materials science with me. I would also like express my sincere gratitude to Dr. James Rigsbee for introducing me to the folks at the Center for Additive Manufacturing and Logistics. Finally, I want to acknowledge ATI Specialty Metals for providing materials for this project.

TABLE OF CONTENTS

| | |
|--|-----|
| LIST OF TABLES | vi |
| LIST OF FIGURES | vii |
| | |
| CHAPTER 1: INTRODUCTION..... | 1 |
| | |
| CHAPTER 2: LITERATURE REVIEW..... | 4 |
| 2.1. Titanium and Titanium Alloys | 4 |
| 2.2. β/α Phase Transformation and Microstructure | 7 |
| 2.3. Ti6Al4V | 10 |
| 2.4. Electron Beam Melting Additive Manufacturing of Ti6Al4V | 11 |
| 2.5. Ti6Al4V with Boron Addition..... | 16 |
| | |
| CHAPTER 3: GRAIN REFINEMENT OF ELECTRON BEAM MELT FABRICATED TI6AL4V WITH HYPOEUTECTIC BORON ADDITION | 21 |
| 3.1. Materials and Methodology | 21 |
| 3.1.1. Feedstock Powder characterization..... | 21 |
| 3.1.2. EBM Fabrication | 25 |
| 3.1.3. Metallography | 27 |
| 3.1.4. EBSD | 28 |
| 3.1.5. X-Ray Diffraction..... | 31 |
| 3.1.6. Electron Microscopy | 32 |
| 3.1.7. Chemical Analysis..... | 32 |
| 3.2. Results | 33 |
| 3.2.1. Powder Analysis | 33 |
| 3.2.2. Metallography | 36 |
| 3.2.3. EBSD | 38 |
| 3.2.4. X-Ray Diffraction..... | 44 |
| 3.2.5. Electron Microscopy | 47 |
| 3.2.6. Chemistry..... | 49 |
| 3.3. Discussion..... | 50 |
| 3.3.1. Powder Analysis | 50 |
| 3.3.2. Microstructural Analysis | 52 |
| 3.3.2.1. Ti6Al4V | 52 |
| 3.3.2.2. Ti6Al4V with Pre-alloyed Boron | 52 |
| 3.3.2.3. Ti6Al4V with Blended Boron | 58 |
| 3.3.3. Chemistry..... | 59 |
| 3.4. Conclusion | 59 |

| | |
|--|---------------|
| CHAPTER 4: MECHANICAL PROPERTIES OF ELECTRON BEAM MELT FABRICATED TI6AL4V WITH BORON ADDITION | 61 |
| 4.1. Materials and Methodology | 61 |
| 4.1.1. Vickers Microhardness | 61 |
| 4.1.2. Flexural Testing..... | 62 |
| 4.1.3. Tensile Testing | 64 |
| 4.1.4. Electron Microscopy | 66 |
| 4.2. Results | 66 |
| 4.2.1. Mechanical Properties | 66 |
| 4.2.2. Optical Microscopy | 70 |
| 4.2.3. Electron Microscopy | 70 |
| 4.3. Discussion..... | 72 |
| 4.3.1. Hardness..... | 72 |
| 4.3.2. Elastic Modulus..... | 74 |
| 4.3.3. Ductility | 75 |
| 4.3.4. Tensile Strength | 76 |
| 4.4. Conclusions | 76 |
| CHAPTER 5: CONCLUSION..... | 78 |
| 5.1. Summary..... | 78 |
| 5.2. Future Work..... | 80 |
| REFERENCES..... | 83 |
| APPENDIX..... | 86 |
| Appendix..... | 87 |

LIST OF TABLES

| | | |
|-----------|---|----|
| Table 3.1 | Ti6Al4V+B pre-alloyed and blended combinations used..... | 22 |
| Table 3.2 | Parameters used for ion milling of EBSD samples..... | 31 |
| Table 3.3 | Important EBSD parameters used..... | 31 |
| Table 3.4 | Pre-alloyed and blended powder size analysis, d50 in μm | 34 |
| Table 3.5 | Average grain width, in μm , measured from optical micrographs for pre-alloyed and blended Ti6Al4V+B | 37 |
| Table 3.6 | Average grain size (μm^2) measured from the bulk of pre-alloyed Ti6Al4V+B microscopy bars. Standard deviation, minimum grain size, maximum grain size, grain count and the 95% confidence interval are reported | 42 |
| Table 3.7 | Average α grain size (μm^2) measured from the bulk of blended Ti6Al4V+B microscopy bars. Standard deviation, minimum grain size, maximum grain size, grain count and the 95% confidence interval are reported | 42 |
| Table 3.8 | ICP and combustion chemical analysis data for blended and pre-alloyed Ti6Al4V+B samples | 50 |
| Table 4.1 | Milling parameters for Ti6Al4V and Ti6Al4V+B flexure bars..... | 63 |
| Table 4.2 | Vickers hardness, flexural modulus, ultimate tensile stress and percent area reduction data for Ti6Al4V and Ti6Al4V+B with a 95% confidence interval.... | 67 |
| Table A.1 | Peak list for titanium. Reference code 00-001-1197 | 87 |
| Table A.2 | Peak list for TiB. Reference code 00-006-0641..... | 87 |

LIST OF FIGURES

| | | |
|------------|--|----|
| Figure 2.1 | Depicts the impact of neutral, α -stabilizing and β -stabilizing alloy elements on the titanium phase diagram. Recreated from Leyens, 2003 | 6 |
| Figure 2.2 | Optical micrograph showing Widmanstätten microstructure in electron beam melt fabricated Ti6Al4V with white α laths nucleated within the darker β phase. Parameters used for ion milling of EBSD samples..... | 8 |
| Figure 2.3 | Illustration showing microstructural evolution in Ti6Al4V during cooling from above the β transus. The final microstructure consists of α laths (white) within the prior β phase (gray). Recreated from Donachi, 2000 | 9 |
| Figure 2.4 | Components of an EBM machine. Recreated from http://www.arcam.com/technology/electron-beam-melting/hardware/ | 14 |
| Figure 2.5 | Prior β grains contain interpenetrating α laths; they span multiple build layers in EBM built Ti6Al4V | 15 |
| Figure 2.6 | A portion of the Ti-B phase diagram showing the phases within areas with <50wt% boron. Recreated from Roy, 2011 | 18 |
| Figure 3.1 | Microtrac TurboTrac at North Carolina State University | 23 |
| Figure 3.2 | Microtrac operating procedure parameters: Analysis options | 23 |
| Figure 3.3 | Microtrac operating procedure parameters: Particle Information..... | 24 |
| Figure 3.4 | Microtrac operating procedure parameters: Perspective..... | 24 |
| Figure 3.5 | Photograph showing the samples for a typical Arcam EBM build for Ti6Al4V or Ti6Al4V+B powders. Samples for flexure and tensile testing, EBSD, optical analysis, ICP-MS and combustion analysis are shown..... | 26 |
| Figure 3.6 | Sectioning was performed parallel to the build direction along the dashed line. The inside surface was prepared for optical microscopy | 28 |
| Figure 3.7 | EBSD samples were sectioned into top, middle and bottom portions for analysis. The upper center of the samples was analyzed using EBSD | 30 |
| Figure 3.8 | Pre-build powder size distribution for Ti6Al4V+B pre-alloyed batches..... | 34 |

| | | |
|-------------|---|----|
| Figure 3.9 | Pre-build powder size distribution for Ti6Al4V+B blended batches | 35 |
| Figure 3.10 | a) Ti6Al4V powder particle, b) Ti6Al4V+1.0B powder particle, c) Ti6Al4V+0.3B powder particles, and d) powder defects | 35 |
| Figure 3.11 | Grain structure in Ti6Al4V and pre-alloyed Ti6Al4V+0.25B, Ti6Al4V+0.5B and Ti6Al4V+1.0B EBM samples | 37 |
| Figure 3.12 | Grain structure in Ti6Al4V and blended Ti6Al4V+0.1B, Ti6Al4V+0.2B and Ti6Al4V+0.3B EBM samples | 38 |
| Figure 3.13 | 220x220 μm EBSD maps of Ti6Al4V and pre-alloyed Ti6Al4V+B with the Euler coloring | 40 |
| Figure 3.14 | 220x220 μm EBSD maps of Ti6Al4V and blended Ti6Al4V+B with the Euler coloring | 41 |
| Figure 3.15 | Displays average α grain size in μm^2 as a function of pre-alloyed boron content (95% confidence interval) | 43 |
| Figure 3.16 | Displays average α grain size in μm^2 as a function of blended boron content (95% confidence interval) | 43 |
| Figure 3.17 | XRD spectra for Ti6Al4V and pre-alloyed Ti6Al4V+B samples | 45 |
| Figure 3.18 | XRD spectra for Ti6Al4V and blended Ti6Al4V+B samples | 46 |
| Figure 3.19 | Development of TiB peak at 42.6deg in Ti6Al4V+B | 47 |
| Figure 3.20 | BSE images of Ti6Al4V and pre-alloyed Ti6Al4V+B. Dark areas <1 μm were imaged in all samples with boron addition | 48 |
| Figure 3.21 | BSE images of Ti6Al4V and blended Ti6Al4V+B. Dark regions <1 μm were imaged in all samples with boron addition | 49 |
| Figure 3.22 | Constitutional supercooling takes place when liquid temperature (T_L) is lower than equilibrium solidification temperature (T_e). Changes in solidification temperature are caused by differences in solute concentration (X_L). Recreated from Callister, 2014 | 54 |
| Figure 3.23 | Microstructural evolution of Ti6Al4V+B in castings | 55 |

| | | |
|-------------|---|----|
| Figure 3.24 | Predicted microstructural evolution of a single layer in EBM fabricated Ti6Al4V+B | 57 |
| Figure 4.1 | Flexure bar sample dimensions after milling..... | 63 |
| Figure 4.2 | Photograph of 4-point bend setup where L_i is 1in, L is 5.5in and d is 0.24in | 64 |
| Figure 4.3 | Tensile bar sample dimensions after milling | 65 |
| Figure 4.4 | Tool room mill set-up for tensile bar machining | 65 |
| Figure 4.5 | Tensile testing setup..... | 66 |
| Figure 4.6 | Changes in microhardness with pre-alloyed boron content in Ti6Al4V (95% confidence interval) | 68 |
| Figure 4.7 | Changes in microhardness with blended boron content in Ti6Al4V (95% confidence interval) | 68 |
| Figure 4.8 | Changes in percent area reduction with pre-alloyed boron content in Ti6Al4V (95% confidence interval)..... | 69 |
| Figure 4.9 | Changes in percent area reduction with blended boron content in Ti6Al4V (95% confidence interval)..... | 69 |
| Figure 4.10 | Machined tensile bar surfaces of Ti6Al4V+0.5B revealing areas containing a) voids evident by un-melted powder particles and b) layer delamination | 70 |
| Figure 4.11 | Fracture surfaces of a) and b) Ti6Al4V+0.50B, c) Ti6Al4V+1.0B and d) Ti6Al4V+0.2 showing regions of un-melted powder particles. Scale bars measure Build direction is horizontal to the page. Scale bars for a-d read 500 μ m, 100 μ m, 100 μ m and 100 μ m, respectively | 71 |
| Figure 4.12 | Voids in Ti6Al4V+B..... | 72 |

CHAPTER 1: INTRODUCTION

Additive manufacturing (AM) is defined by ASTM F2792 as the process of joining materials to make objects from 3D model data, layer upon layer, unlike subtractive manufacturing methodologies. The layer-by-layer process removes many geometric limitations present in traditional manufacturing methods. Complex structural designs allowable by AM inspire the production of lightweight, high-strength structures for the aerospace and automotive industries. However, limited data are available regarding the metallurgical characteristics that characterize AM processes.

Electron beam melting (EBM), from Arcam (Möndal, Sweden) is an AM powder bed fusion process in which metal powders are selectively melted by an electron beam. For titanium alloy Ti6Al4V, the EBM process produces structures with mechanical properties rivaling that of cast components. Ti6Al4V fabricated with EBM exhibits an inhomogeneous and columnar microstructure perpendicular to build direction. While directional anisotropy may be desirable for certain applications, in others a more isotropic and refined microstructure may be required. Therefore, engineering of microstructure has been a topic of recent interest, particularly in light of the significant level of control of over thermal histories and local environment afforded by EBM. For instance, several groups have recently shown that for nickel alloy 718 local changes in beam energy density and thus cooling rates, can lead to tailored microstructures within a single component [Helmer, 2014; Sames, 2014,].

However, for the Ti6Al4V system, the processing window of feasible beam velocity and current combinations may not permit such freedom of microstructural design necessitating alternate approaches. Grain refinement in cast titanium alloys has previously been investigated through the addition of hypoeutectic concentrations of boron [Luan, 2014; Luan, 2015; Roy, 2011; Sen, 2007; Sen, 2010; Sen and Ramamurty, 2010; Tamirisakandala, 2003; Tamirisakandala, 2005; Zhu, 2003]. The objective of this work is to explore the use of boron additions as a means of refining the microstructure in electron beam additive manufacturing of Ti6Al4V, and to study its influence on the bulk mechanical properties of the material. For this study, Ti6Al4V+B alloy samples were fabricated using pre-alloyed powder feedstock materials with boron weight fractions of 0.25, 0.50 and 1.0%. An additional set of compositions was fabricated by blending various concentrations of Ti6Al4V+1.0B and Ti6Al4V powders to produce bulk chemistries with boron weight fractions of 0.10, 0.20 and 0.30%. In both the pre-alloyed and blended powders, increasing boron additions are hypothesized to progressively refine the relatively coarse columnar grain structure of EBM fabricated Ti6Al4V, increase strength and reduce ductility.

This thesis is organized into five chapters. **Chapter 2** provides a review of the processing and characteristics of the pertinent titanium alloys, the electron beam melting process, and the role of boron in the refinement of microstructure for Ti6Al4V castings. **Chapter 3** describes the influence of boron additions on the grain size of electron beam additively manufactured Ti6Al4V. **Chapter 4** describes the influence of boron additions on

the mechanical properties of electron beam additively manufactured Ti6Al4V. **Chapter 5** presents a detailed discussion of this work and proposes opportunities for future investigations.

CHAPTER 2: LITERATURE REVIEW

2.1. Titanium and Titanium Alloys

Titanium is the fourth most abundant structural metal in the earth's crust following aluminum, iron and magnesium. Despite this, titanium is rarely found in economically extractable concentrations or in a pure state. Concentrated sources of the element are found and extracted from several minerals including ilmenite, titanomagnetite, rutile, anatase and brookite. Due to its limited availability in the pure state, applications of pure titanium are limited to experimentation and research [Boyer, 1994]. Titanium is a transition metal with an incomplete outer shell in its electronic structure allowing the element to form stable compounds with substitutional elements within a $\pm 20\%$ size factor [Polmear, 1996]. Alloys of titanium are marked by two key properties: high specific strength and exceptional corrosion resistance. These properties explain the prominent use of titanium alloys in the aerospace, chemical, biomedical and marine industries [Leyens, 2003].

Titanium crystallizes in the hexagonal close packed structure (hcp) at temperatures below 882°C ; this is called alpha (α) titanium. At temperatures above 882°C , pure titanium undergoes an allotropic phase change from α hcp titanium to beta (β) body centered cubic (bcc) titanium. The temperature at which the α/β transition occurs is known as the β transus temperature. The α/β phase transformation that occurs in titanium is the basis for the wide range of properties seen in its alloys [Leyens, 2003]. Alloy elements introduced into titanium

are classified into three categories: α -stabilizers, β -stabilizers and neutral elements, depending on which titanium phase they stabilize. Alpha-stabilizers expand the α phase of titanium to higher temperatures by raising the β transus temperature [Boyer, 1994]. Elements classified as β -stabilizers extend the β phase region in titanium by lowering the β transus temperature [Leyens, 2003]. An element that has no significant effect on the β transus is classified as a neutral element. Examples of neutral elements added to titanium include Zr, Sn and Si [Polmear, 1996].

Alloys of titanium containing α -stabilizers are classified as α -alloys. Alpha-stabilizers are solutes that preferentially dissolve in the hcp α phase of titanium. Elements defined as α -stabilizers include Al, O, N and C [Polmear, 1996]. The addition of α -stabilizers to titanium creates a dual phase $\alpha+\beta$ region on the titanium phase diagram, as seen in Figure 2.1 [Leyens, 2003]. Since the hcp phase is stable at normal temperatures (excluding those that are very high), α -alloys do not exhibit a ductile to brittle transition, a property found in bcc structures. Because α -alloys do not exhibit brittleness at low temperatures, they are often used in low temperature applications [Boyer, 1994]. Alpha-alloys are also credited for their excellent resistance to corrosion and oxidation; accordingly, they are useful materials in the chemical and process engineering industries [Polmear, 1996].

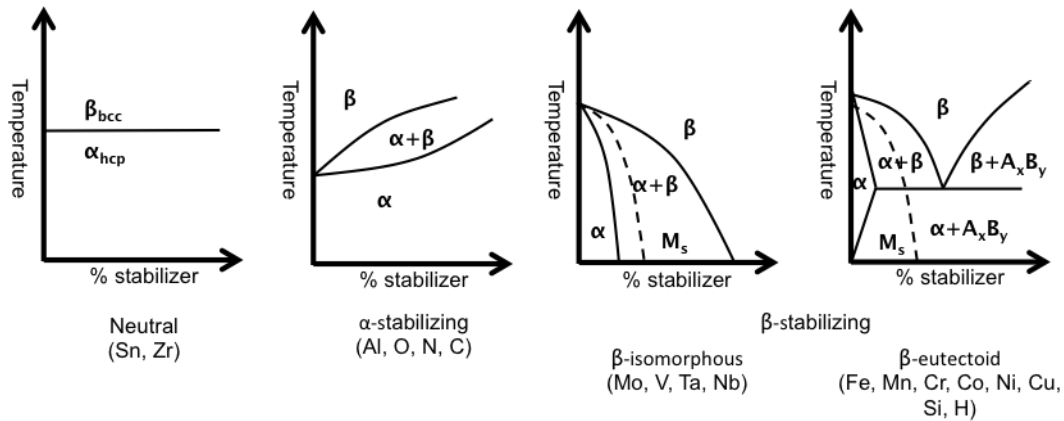


Figure 2.1. Depicts the impact of neutral, α -stabilizing and β -stabilizing alloy elements on the titanium phase diagram. Recreated from Leyens, 2003.

Alloys that contain β -stabilizers are known as β -alloys. Beta-alloys are categorized as either β -isomorphous or β -eutectoid [Boyer, 1994]. Mo, V, Nb and Ta are β -isomorphous elements; these elements are soluble in β titanium, so the β -transus continues to decrease as higher weight percent of the β -stabilizers is added. However, β -eutectoid elements like Fe, Mn, Cr, Co, Ni, Cu, Si and H, are not as soluble in β titanium, instead they form intermetallic compounds through eutectoid decomposition of the β -phase [Ezugwu, 1997; Leyens, 2003]. Beta-alloys have the highest strength to weight ratio of all the titanium alloy classes; they provide an ideal combination of strength, toughness and fatigue resistance for specific applications. However, β -alloys are not suitable for low temperature applications due to their ductile to brittle transition [Boyer, 1994].

Alpha+beta alloys are the most prominently used titanium alloy group. These alloys contain α -stabilizers and between 4 and 6wt% β -stabilizers; subsequently, the α and β phases coexist in the microstructure at room temperature [Boyer, 1994]. Alpha+beta alloys exhibit high strength and good manufacturability at room temperature. The microstructure and mechanical properties of $\alpha+\beta$ alloys can be controlled through heat treatment of the $\alpha+\beta$ alloys. Ti6Al4V is the most widely used $\alpha+\beta$ alloy [Boyer, 1994].

2.2. β/α Phase Transformation and Microstructure

The microstructure of titanium alloys is described by the size, shape and arrangement of the α and β phases. Thermal history during solidification is a key factor influencing final microstructure, which affects the mechanical properties of the material. Post processing factors, mainly thermomechanical treatments, also alter the final microstructure of titanium alloys [Sen and Ramamurty, 2010]. In titanium, primary β grains nucleate and grow during cooling. As temperature decreases below the β transus, the α phase nucleates at the prior β grain boundaries [Donachi, 2000]. These nuclei grow as parallel plates having the same crystal orientation within the β matrix; this is called the lamellar structure.

A group of lamellae with the same crystal orientation forms a colony. Colonies grow within a single β grain until they come into contact with other α colonies. Cooling rate and prior β boundary size dictate the coarseness of α colonies; faster cooling rates lead to a finer and thinner lamellae structure. Decreasing colony size improves the yield strength, ductility

and resistance to crack propagation in an alloy [Pederson, 2002]. Interpenetrating lamellar structures with different orientations produce the “basket weave” or Widmanstätten microstructure, shown in Figure 2.2, which is characteristic of titanium alloys [Leyens, 2003]. The formation of the Widmanstätten microstructure during cooling from above the β transus is illustrated in Figure 2.3.

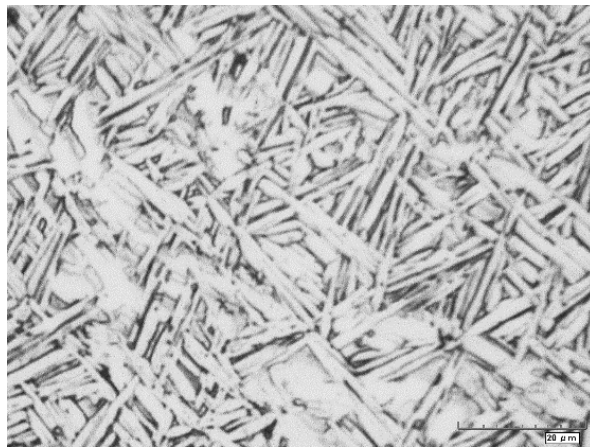


Figure 2.2. Optical micrograph showing Widmanstätten microstructure in electron beam melt fabricated Ti6Al4V with white α laths nucleated within the darker β phase.

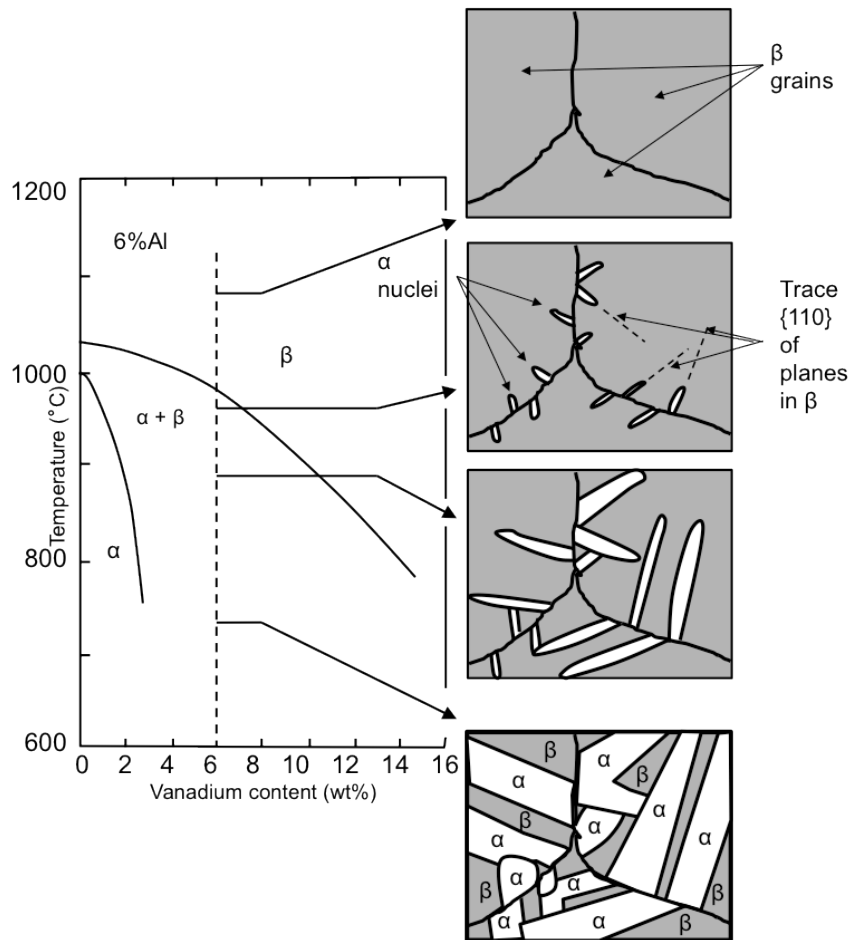


Figure 2.3. Illustration showing microstructural evolution in Ti6Al4V during cooling from above the β transus. The final microstructure consists of α laths (white) within the prior β phase (gray). Recreated from Donachi, 2000.

2.3. Ti6Al4V

Ti6Al4V is the most widely used titanium alloy accounting for more than 50% of total titanium alloy production [Leyens, 2003]. Ti6Al4V contains 6wt% aluminum, an α -stabilizer, and 4wt% vanadium, a β -stabilizer, so both α and β phases are present in the microstructure at room temperature [Polmear, 1996]. Ti6Al4V is designed for use in high strength applications from low to moderate temperatures up to 400°C [Ezugwu, 1997]. Ti6Al4V ingots are typically fabricated using vacuum arc remelting (VAR). VAR allows for precise control over the melt temperature of molten Ti6Al4V, which is solidified in water-cooled copper crucibles. The microstructure generated is strongly dependent on the cooling rate. Therefore, the melting power of the VAR, thermal properties of Ti6Al4V and heat transfer between the ingot and the crucible influence final structure. As such, the microstructure of cast ingots is divided into three separate zones:

1. The chill zone is the outer surface of the ingot where rapid cooling gives rise to fine equiaxed grains [Pederson, 2002].
2. As heat is dissipated, grains begin to grow through the bulk of the material parallel to the temperature gradient. This is named the columnar zone [Pederson, 2002].
3. Finally, the equiaxed zone is in the center of the ingot. Macroseggregation of β -stabilizers lower the melting point of the center of the ingot leading to a homogeneous and equiaxed grain structure. [Pederson, 2002].

Conventionally cast Ti6Al4V parts have relatively coarse, anisotropic grains and a strong texture component, both undesirable for in-service and fracture-critical applications. For this reason, extensive hot working in the β -phase field, or thermo-mechanical processing (TMP), is needed to reduce the grain size after casting. The TMP post-processing step results in high-energy consumption and yield loss making finished Ti6Al4V parts comparatively expensive [Donachie, 2000; Sen and Ramamurty, 2010; Tamirisakandala, 2005].

2.4. Electron Beam Melting Additive Manufacturing of Ti6Al4V

AM applications have recently begun to shift from predominantly rapid prototyping to the manufacturing of end-use parts. AM offers several advantages over traditional manufacturing including design flexibility and efficient material utilization [Guo, 2013]. In practice, AM is performed using the following steps:

1. A 3D computer aided design (CAD) file is generated of the part to be built.
2. The CAD file is converted into a standard tessellation language (.STL) file, which closely approximates the geometry using triangles.
3. The .STL file is sliced into layers to be read by the 3D printer; orientation and scaling are chosen in the AM software.
4. Layers are consolidated using thermal energy, light or binder.
5. The completed part can be subject to post processing steps.

Electron beam melting (EBM), depicted in Figure 2.4, is a powder bed fusion AM process used to construct metal parts. A focused electron beam is used to selectively scan a powder bed following sliced data from a CAD file. The kinetic energy of the electrons is converted into thermal energy, and metallic powder is locally melted to form a single layer of the build file. An EBM machine is comprised of three major components, an electron gun, a build tank and a vacuumed chamber. In the electron gun, electrons are boiled off a tungsten filament; magnetic lenses focus and direct the electron beam onto the powder bed. The powder bed, along with the start plate and build platform, is contained within the build tank. The first layer of powder is melted onto the start plate. The role of the build platform is to lower the start plate, so a rake can recoat the powder bed with a fresh layer of powder. Powder is kept in hoppers on either side of the build tank in the vacuumed chamber. Several alloys used in EBM have a high reactivity, so the process is completed under vacuum. The vacuum chamber also prevents energy loss in the electron beam.

The electron gun column houses a ~4.5 kW thermionic tungsten filament under a vacuum of about 6×10^{-6} mbar and typically uses an accelerating potential of 60 kV. Astigmatism correction, focus and deflection coils form the electrons into a narrow high-energy beam that is guided across the powder surface. The energy density within the electron beam can be as high as 106 kW/cm^2 . The system vacuum level is maintained by a controlled vacuum system that introduces small quantities of inert gas into the build area. The vacuum chamber, which maintains an internal pressure of 2×10^{-3} mbar, contains the build tank and powder

dispatching system. Spherical powder is spread onto the build surface by the dispatching system. Initially, the beam scans the surface of the start plate at relatively high power and speed (~33 mA and ~15 m/s) raising the temperature of the powder bed to ~760 °C. The next step, melting, is divided into two sub-steps, contours and hatching. The contours step uses a relatively low current and speed (~4 mA, 340 mm/s) to trace the outline of each cross sectional layer of the 3D geometry using a proprietary control step called “multi-beam”.

This utilizes the high scan rate capabilities to jump between multiple locations on the contour approximating multiple beams which are able to simultaneously maintain multiple melt pools. This approach has improved surface finish (over single spot contouring) while maintaining productivity. The second component of the melt theme is the “hatch” step. Here, the beam current and speed are increased (~15 mA, 4530 mm/s) and the beam is guided in a raster pattern to fully melt and densify the area between the contours. The build table is lowered by a fixed increment (50-70 μ m), new powder is deposited, and the process repeats for the next cross section of the 3D geometry. After all layers have been fabricated, the chamber is allowed to slowly cool back down to room temperature. Parts fabricated are fully dense if processing conditions are optimized [Murr, 2009].

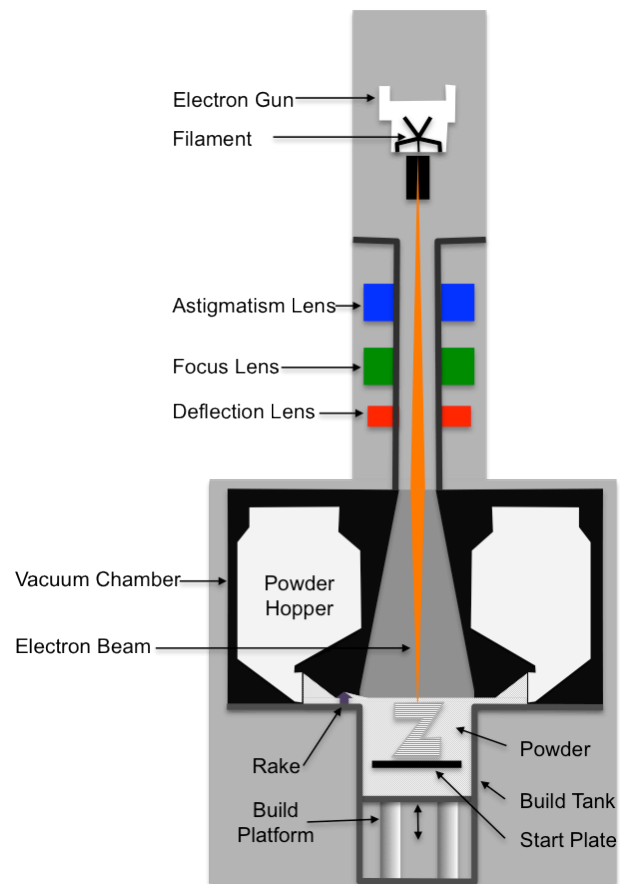


Figure 2.4. Components of an EBM machine. Recreated from <http://www.arcam.com/technology/electron-beam-melting/hardware/>.

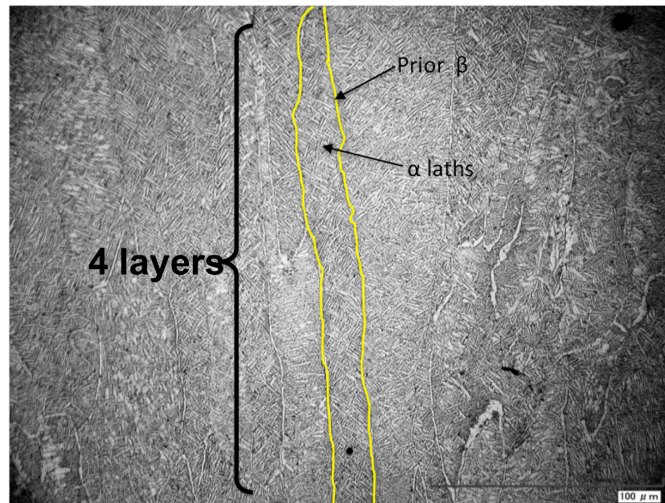


Figure 2.5. Prior β grains contain interpenetrating α laths; they span multiple build layers in EBM built Ti6Al4V.

The layer-by-layer melt/solidification process and the continuously moving melt/solidification front differ fundamentally from solidification in conventional metallurgical processes. During the melting of a single layer, several layers below it are re-melted; this promotes the continuous growth of grains that can span several layers along the build axis (Figure 2.5). Furthermore, the build chamber is held at relatively high temperatures ($\sim 700^{\circ}\text{C}$) until the entire build is completed. This induces mechanical changes including annealing and the eradication of thermally induced dislocations, comparable to TMP treatments in traditional metallurgy [Al-Bermani, 2010; Murr, 2015]. In one study, mechanical properties of Arcam EBM fabricated Ti6Al4V were compared against Ti6Al4V prepared by laser deposition, casting and forging processes. Results indicated that Arcam EBM Ti6Al4V alloys meet and often exceed the mechanical properties of more traditional

metallurgy methods. Additionally, Arcam EBM Ti6Al4V fulfills requirements in accordance with several Aerospace Material Specification and American Society for Testing and Materials specifications for Ti6Al4V [Bass, 2008].

2.5. Ti6Al4V with Boron Addition

The addition of trace amounts of inoculants to metal is a commonly used process to accelerate nucleation and reduce grain growth. Stable insoluble particles in molten metal act as nucleation sites for grains and accelerate heterogeneous nucleation [Sen, 2013]. In 2003, Zhu et al. observed a refinement in the microstructure of Ti6Al4V while studying the effects of boron addition on the mechanical properties of Ti6Al4V dental implants [2003]. The decrease in grain size was attributed to the precipitation of TiB needles acting as nucleation sites for additional β grains. The Ti-B phase diagram, illustrated in Figure 2.6, shows that TiB forms after primary β grains nucleate; therefore, TiB cannot act as a nucleation site. In 2005, Tamirisakandala et al. validated the use of boron to refine the grain structure of Ti6Al4V. The addition of 0.10wt% boron reduced the average prior β boundary size in Ti6Al4V from 1700 μm to 200 μm [2005]. In another instance, Roy et al. reported a decrease in prior β boundary size from 1720 μm to 381 μm and α colony size from 163 μm to 61 μm with additions of 0.10wt% boron in cast Ti6Al4V [2011]. Minimal reduction in grain size was observed past 0.10wt% boron due to the saturation of the growth restriction factor according to Equation 1 [Tamirisakandala, 2003].

Equation 1:

$$Q = m(k - 1)C_0$$

The growth restriction factor (Q) is a function of the solute content (C_0), the slope of the liquidus line (m) and solute partition coefficient (k) [Tamirisakandala, 2003].

Microstructural analysis of Ti6Al4V+B castings reveals a classic Widmanstätten microstructure [Roy, 2011]. Final grain size of the α and β phases is determined by the competition between nucleation and growth rates of primary β grains. Tamirisakandala et al have suggested that the rejection of boron from primary β grains during growth leads to a constitutionally supercooled melt that restricts grain growth and enhances nucleation [2005]. Accumulation of boron in the constitutionally supercooled melt results in the formation of TiB around prior β grain boundaries [Roy, 2011; Tamirisakandala, 2005; Zhu, 2003;].

TiB needles act as grain boundary pinning points and limit the inhomogeneous growth rate of β grains despite elevated temperatures [Roy, 2011]. Increased nucleation, decreased growth rate and TiB pinning points promote the formation of more equiaxed and refined prior β grain boundaries in Ti6Al4V+B. Reduction in α size is a product of increased nucleation on the energetically preferred TiB/ β interface and the decrease in primary β size [Sen, 2007].

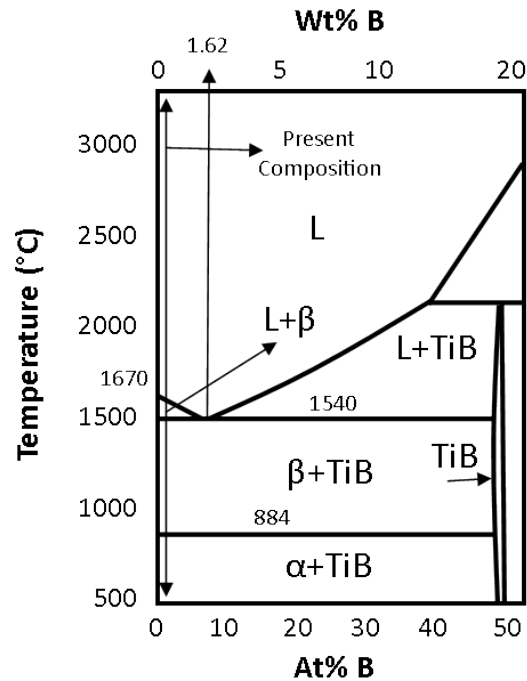


Figure 2.6. A portion of the Ti-B phase diagram showing the phases within areas with <50wt% boron. Recreated from Roy, 2011.

Ti6Al4V castings often exhibit poor room-temperature ductility with elongation to failure of less than 5%. Poor ductility is a result of the coarse grain structure and the weak cohesion between prior β grain boundaries. Several researchers have reported increased ductility and strengths in boron-modified Ti6Al4V [Luan, 2014; Luan, 2015; Sen, 2007; Tamirisakandala, 2003]. Experiments by Sen et al. on Ti6Al4V with 0.05, 0.10 and 0.40wt% boron additions demonstrated enhanced elastic modulus, yield strength and ultimate tensile strength (UTS) values. A majority of the improvement in mechanical properties occurred within the first additions of boron up to 0.10wt%. Further additions of boron continued to improve strength properties, but saturation in the mechanical improvement was observed [2007]. Earlier work

by Tamirisakandala et al. resolved that Ti6Al4V+B strengthens by two mechanisms: load sharing with the high strength TiB phase and strengthening via the Hall-Petch mechanism [2003]. At high boron concentrations (1.6wt%) TiB load sharing dominated strength improvement in Ti6Al4V+B. The strengthening effect of refined grains through the Hall-Petch mechanism was neglected due to the high volume fraction of TiB [Tamirisakandala, 2003]. Sen et al. predicted that the contributions from the Hall-Petch strengthening mechanism (Equation 2) would dominate over the load-sharing component in Ti6Al4V+B if boron additions were below 0.04wt% [2007]. A strong correlation between σ_y and β/α grain diameter was revealed, therefore the authors concluded that enhancement in strength at low boron concentration is due to the Hall-Petch strengthening mechanism [Sen, 2007].

Equation 2:

$$\sigma_y = \sigma_0 + \frac{k_y}{\sqrt{d}}$$

Where σ_y is the yield stress, σ_0 is stress for dislocation movement to occur, k_y is a strength coefficient and d is grain size.

In addition to increased strength, an enhancement in the strain to failure (i.e. ductility) was observed in samples with 0.05wt% boron additions. Ductility enhancement with low boron addition was attributed to the microstructural refinement of Ti6Al4V. At larger boron additions the brittle TiB phase around the grain boundaries tends to reduce ductility [Sen, 2007].

Luan et al. reported an increase in average yield strength, ultimate tensile strength and percent elongation (from 4% to 9%) with only 0.02wt% boron in Ti6Al4V. Fracture surface analysis revealed that without boron the Ti6Al4V fracture mechanism is fully intergranular (i.e. follows the grain boundaries), while the Ti6Al4V+B samples showed almost fully transgranular fracture (follows the lattice and ignores grain boundaries). Changes in fracture mode cannot be fully explained by grain refinements; it is likely that grain boundary cohesion is enhanced by the boron additions. If the cohesion effect on grain boundaries is larger than embrittlement of the TiB phase in these small additions, ductility is enhanced [2015].

CHAPTER 3: GRAIN REFINEMENT OF ELECTRON BEAM MELT FABRICATED Ti6Al4V WITH HYPOEUTECTIC BORON ADDITION

Grain refinement of Ti6Al4V via hypoeutectic boron additions is well documented for Ti6Al4V castings. In this chapter, the effects of various boron contents on grain size in Ti6Al4V+B are investigated for powders used in EBM additive manufacturing. It is predicted that with increasing boron content a corresponding reduction of grain size and homogenization of the microstructure will be observed. Samples were fabricated using an Arcam A2 EBM SP2 with parameters optimized for Ti6Al4V. Sample microstructure was evaluated using optical microscopy, scanning electron microscopy (SEM) and electron backscatter diffraction (EBSD). X-ray diffraction (XRD) was used for phase identification, and compositional analysis was performed by inductively coupled plasma mass spectrometry (ICP-MS) and combustion analysis.

3.1. Materials and Methodology

3.1.1. Feedstock Powder characterization

Argon gas atomized Ti6Al4V powder with a nominal size fraction between 45-105 μ m was produced by ATI Specialty Metals (Robinson, PA). In this study, two distinct pathways have been explored; one using powders pre-alloyed with boron (0.25, 0.5 and 1.0% wt.) and another in which Ti6Al4V powder was blended with Ti6Al4V1B powder to achieve various bulk chemistries (0.1, 0.2 0.3% wt.). These powders were blended in a rotary barrel (Arcam,

Möndal, Sweden) for 30 minutes. Table 3.1 delineates the pre-alloyed and blended powder combinations used in this study.

A Microtrac Turbotrac S3500 laser diffraction particle size analyzer (Montgomeryville, PA), depicted in Figure 3.1, was used to quantify the size distribution of each powder batch. Powder samples (~50g) were collected from each batch before powder was put into the build chamber. Parameters were set such that analysis was performed dry, the particle shape was ‘irregular’, and the transparency was ‘absorbing’. Data represented the number distribution of powder size. The software noise filter was also disabled. Operating parameter screen shots are shown in Figures 3.2-3.4.

Table 3.1. Ti6Al4V+B pre-alloyed and blended combinations used.

| Pre-alloyed | Blended |
|--------------------|----------------|
| Ti6Al4V + 0B | Ti6Al4V + 0B |
| Ti6Al4V + 0.25B | Ti6Al4V + 0.1B |
| Ti6Al4V + 0.5B | Ti6Al4V + 0.2B |
| Ti6Al4V + 1.0B | Ti6Al4V + 0.3B |



Figure 3.1. Microtrac Turbotrac at North Carolina State University.

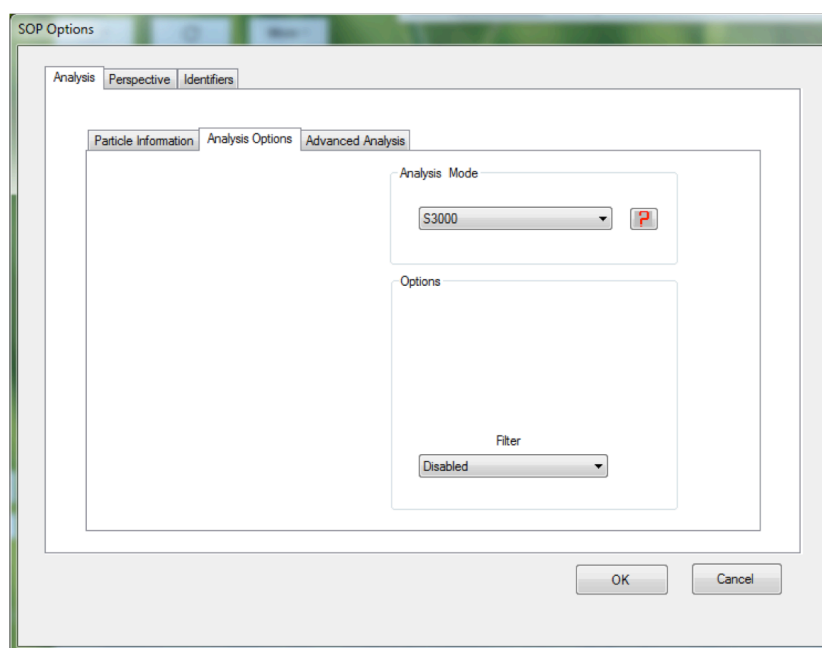


Figure 3.2. Microtrac operating procedure parameters: Analysis options.

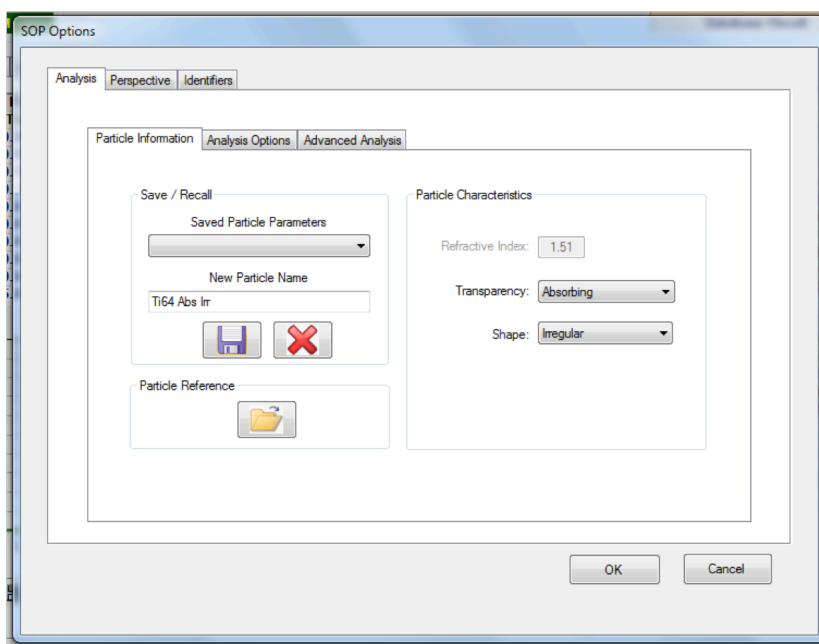


Figure 3.3. Microtrac operating procedure parameters: Particle Information.

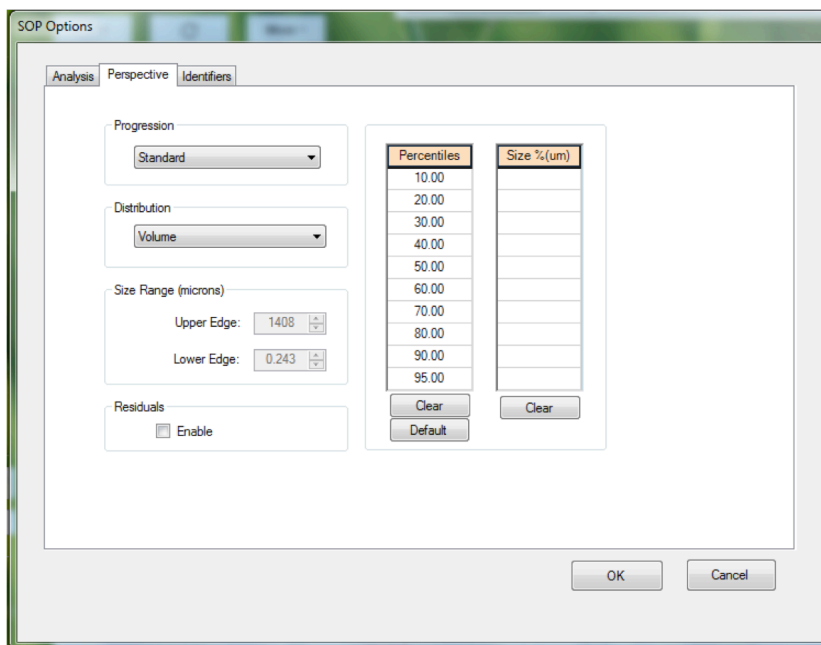


Figure 3.4. Microtrac operating procedure parameters: Perspective.

Powder samples were also mounted in trans optic mounting powder and progressively ground with 120, 240, 320, 400, 600, 1000 and 2000 grit grinding paper. After a final polishing using 0.3 μ m alumina slurry, samples were rinsed in acetone and prepared for microscopy by etching with Kroll's reagent (2% HF, 5% HNO₃, 93% distilled water) for 7-12 seconds. Powder microstructures were observed using the Hirox KH-7700 (Hackensack, NJ) digital light microscope with the MX(G)-10C lens and OL-350(II) adapter. Powder defects produced during atomization, such as satellites and gas entrapments, were analyzed. The circulation of gas inside the atomization chamber lifts finer particles that collide with and attach to larger molten particles. Fine particles attached to coarser particles are called satellites. Furthermore, powder defects can also be caused by the entrapment of gas within a powder particle during atomization. Both powder defects were examined.

3.1.2. EBM Fabrication

Seven EBM builds were produced in the Arcam A2 EBM (Möndal, Sweden) using blended (n=3) and pre-alloyed (n=3) combinations of Ti6Al4V+B, and Ti6Al4V (n=1) as a control. Parameter set Ti6Al4V-Melt-50 optimized for Ti6Al4V by Arcam AB in 2013 were used for each build. The nominal layer thickness was 50 μ m. Sample build geometries were constructed and arranged in Magics (version 19.02), then sliced in the Arcam Build Assembler.

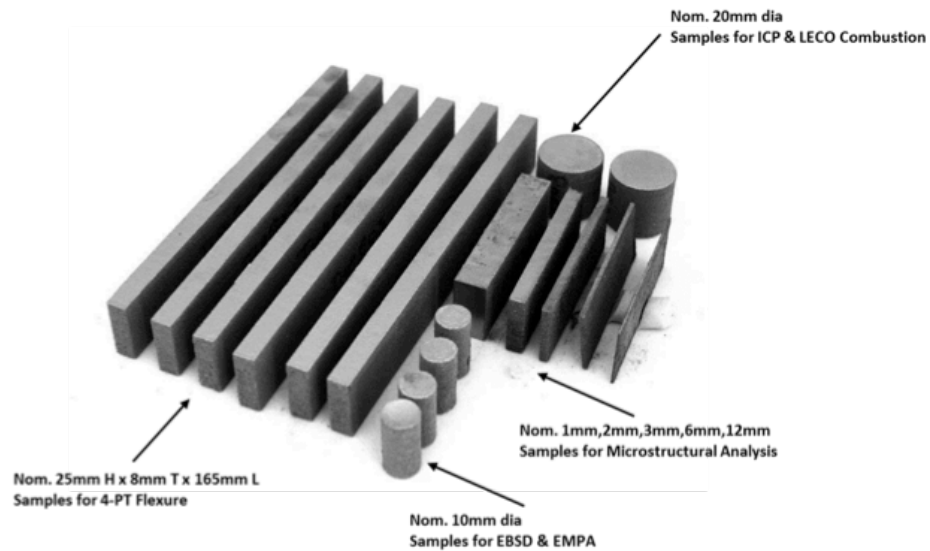


Figure 3.5. Photograph showing the samples for a typical Arcam EBM build for Ti6Al4V or Ti6Al4V+B powders. Samples for flexure and tensile testing, EBSD, optical analysis, ICP-MS and combustion analysis are shown.

A photograph representing the layout of each build is shown in Figure 3.5; each of the seven build volumes contained samples for flexure and tensile testing, EBSD, optical analysis, ICP-MS and combustion analysis. A limited amount of powder was available for each build, so flexure, tensile and microstructural samples were oriented in the YZX direction (per ASTM F2921-11^{e2}).

Samples were fabricated directly on stainless (304) steel plates measuring 190 mm x 190 mm x 10 mm with no support structures. The temperature at the start of the build, as measured by a thermocouple at the bottom of the starting plate, was 760°C. After a build was completed, the chamber was allowed to slowly cool back to room temperature. The start

plate was removed from the build tank and placed in the Arcam Powder Recovery System (PRS) where Ti6Al4V powders were accelerated out of an air-powdered pressure gun. Powders were fired at the build plate to break up and remove powders sintered around the fabricated part. After the build plate was clear of non-melted powder, a hammer was gently tapped on the underside of the start plate to remove the samples.

3.1.3. Metallography

Samples built for microstructural analysis were sectioned parallel to the build direction. Sectioning was performed with Mark V Series (East Granby, CT) 600 sectioning saw using a SiC blade. Bars were cut at least 10 mm away from the sample edge, as illustrated in Figure 3.6, and the inside surface was examined. Samples were mounted in phenolic mounting powder and ground and polished following the protocol previously described.

Sample sections were imaged using a Hirox KH-7700 digital light microscope (Hackensack, NJ) with the MX(G)-10C lens and OL-350(II) adapter. Digitally reconstructed and tiled images, with a field of view measuring roughly 5mm, were obtained along the build direction for all sample sections. To account for the high aspect ratio of the prior β grain boundaries, a modification of the linear intercept method was used to estimate prior β grain length and width values from the tiled microscopy images. Ten evenly spaced lines were drawn along the length and width of each image. Along each line, individual grain length/width values were recorded and averaged. In the case that a grain length extended

past the viewing area, values were not recorded; this was the case for Ti6Al4V, and all Ti6Al4V+B pre-alloyed samples. No prior β grain boundaries were distinguishable for the Ti6Al4V+1.0B samples.

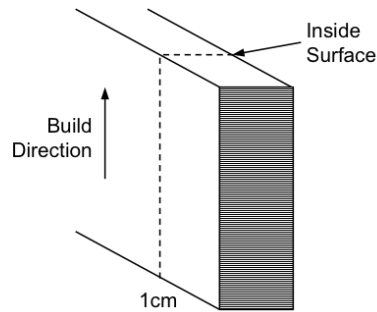


Figure 3.6. Sectioning was performed parallel to the build direction along the dashed line. The inside surface was prepared for optical microscopy.

3.1.4. EBSD

A section, 2-3mm thick was cut from the EBSD sample cylinders using a Bueler Isomet (Lake Bluff, IL) low speed sectioning saw. Slices were sectioned horizontally into bottom, middle, and top sections as illustrated in Figure 3.7. Middle samples were adhered to a phenolic sample mount with cyanoacrylate, ground, polished and etched as described previously. A razor blade was used to gently remove the sample from the mount and each piece (bottom, middle and top) was labeled and notched with the saw blade in the upper left corner to denote sample orientation. After this, samples were adhered to an SEM pin-mount with cyanoacrylate and a colloidal silver paint was used to create a conductive path from the

sample to the pin. Final sample preparation involved a 45-minute ion polish using a Fischione Model 1060 SEM Mill (Export, PA) using parameters outlined in Table 3.2.

Initial EBSD analysis was performed on the top of each bar sample. However, since different thermal histories exist at the top of a build, the images collected did not represent the bulk microstructure in the microscopy bar. For this reason, each middle sample was analyzed using the FEI Quanta 3D FEG dual beam SEM (Hillsboro, OR) with an Oxford (Abingdon, United Kingdom) EBSD detector, to represent the bulk microstructure of the samples.

EBSD parameters were optimized to obtain EBSD maps with less than 13% zero solution points; the general parameters used are delineated in Table 3.3. A small step size, $0.2\mu\text{m}$, was used to ensure adequate resolution of the reduced α grain size given the high boron additions, and the preliminary optical measurements. A small orientation map was taken to ensure that sample preparation and the chosen parameters were sufficient to produce an image with <13% zero solution spots, for which the detector could discern no crystal orientation. If the small map was adequate, $220\times 220\mu\text{m}$ images at 500x magnification were collected from the upper center of each middle sample in an area where a limited number of pores or other surface inconsistencies existed. In case initial EBSD testing showed poor results, samples were put into the ion mill for an additional 45 minutes. Euler images were collected and analyzed.

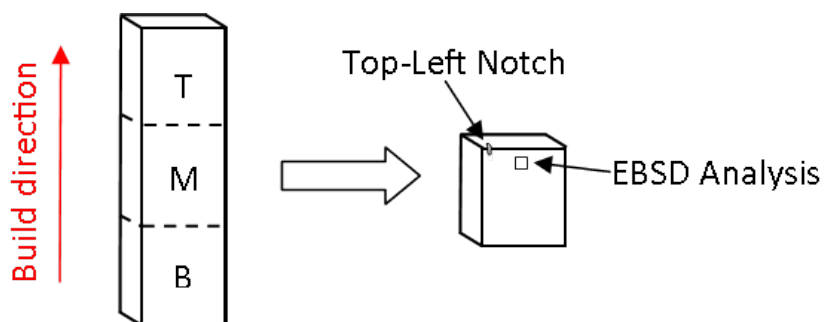


Figure 3.7. EBSD samples were sectioned into top, middle and bottom portions for analysis. The upper center of the samples was analyzed using EBSD.

Grain size was measured using the HKL Channel5 Nanoanalysis software package by Oxford Instruments (version 5.12.52.0). Before grain size measurements were acquired, a noise reduction was performed on the EBSD orientation maps to remove the zero solutions points and incorrectly indexed points (wild spikes). To perform the noise reduction, Scaling was set to 2x, and the All Euler function was selected. Next, the Zero Solution value was set to three marks to the left of high. This means that if a zero solution point is surrounded by an identical orientation, it is filled with that orientation. This algorithm was iterated until no zero solutions spots remained. In addition, wild spikes were corrected by copying the orientation of neighboring points using the Wild Spikes Extrapolate button in the analysis software. Wild spikes are pixels that have a different orientation than all surrounding pixels; these are likely incorrectly indexed by the EBSD software.

After the noise reduction, α grain size was measured. A grain is defined as an area bounded with a mis-orientation angle larger than a set critical value; this value is typically

set to 10° [Schwartz, 2009]. Individual α lath sizes, excluding all border grains, were collected. Grain statistics containing average grain size, variance, standard deviation, coefficient of variation, minimum grain size, maximum grain size and the size of the data set (number of grains) were reported for each Euler image.

Table 3.2. Parameters used for ion milling of EBSD samples.

| | |
|---------------------------|-----------------------|
| Voltage | 4 kV |
| Current | 42.7 μ A |
| Focus | 50% |
| Beam angle | 4 degrees |
| Sample Orientation | Continuously Rotating |

Table 3.3. Important EBSD parameters used.

| | |
|-----------------------------|-------------|
| Accelerating Voltage | 20 Kv |
| Beam Current | 11 nA |
| Binning | 4x4 |
| Dwell Time | 30 sec |
| Step Size | 0.2 μ m |
| Magnification | 500x |

3.1.5. X-Ray Diffraction

X-Ray diffraction (XRD) analysis was performed on the Rigaku SmartLab (Tokyo, Japan) X-ray Diffractometer. XRD spectra were collected for Ti6Al4V and Ti6Al4V+B solid EBSD samples that were removed from the SEM mount and placed on a standard single specimen stage. Bragg-Brentano optics were used and included the following parameters:

- Variable incident slit: 0.05-7.0 mm
- Height limiting slit: 2.0-10.0 mm
- Soller Slits: 5° axial divergence.

Spectra were collected at 2θ ranging from 10° to 90° with a step size of 0.05°.

3.1.6. Electron Microscopy

Polished and etched metallographic samples were examined using a JEOL 6010LA (Tokyo, Japan) SEM in secondary and backscattered electron modes. A representative area of each Ti6Al4V and Ti6Al4V+B sample was imaged at 5000x. Elemental analysis was performed at areas of interest using energy dispersive x-ray spectrometry (EDS).

3.1.7. Chemical Analysis

Chemistry sample cylinders from each build were cut in half parallel to the build direction using the Mark V Series 600 (East Granby, CT) sectioning saw. Sample halves were sent to ATI Specialty Metals (Robinson, PA), where ICP and Combustion analysis were carried out. ICP is an elemental analysis technique in which samples are converted into an aerosol. Atoms within the aerosol are ionized then detected by a mass spectrometer. ICP generally forms positive ions, so elements that prefer to form negative ions or are not easily ionized, are difficult to detect (C, O and N) [Wolf, 2005]. In combustion analysis, samples are burned and the products are collected and weighted. Elemental composition of low mass elements, like C, O and N, are determined.

3.2. Results

3.2.1. Powder Analysis

Median powder size ranged from 104 μm to 134 μm (Table 3.4). The size distributions for each composition are displayed in Figures 3.8 and 3.9. Most powder batches had a median size within $\pm 6\mu\text{m}$ (excluding Ti6Al4V+0.50B) and exhibited a Gaussian distribution. The median size of the Ti6Al4V+0.50B powder was 134 μm , about 20 μm larger than other distributions. Additionally, the Ti6Al4V+0.20B blended powder distribution was skewed to the right compared to the other distributions; however, the median value was similar to other blended powder samples.

Optical analysis of the polished and etched powder samples show substantial differences in microstructure between the control, Ti6Al4V, and the boron modified material. Ti6Al4V powder particles show the typical α lath structure (Figure 3.10a) while the pre-alloyed particles exhibit a homogenous structure with refined, dendritic patterns (Figure 3.10b). Figure 3.10c depicts a blended powder batch containing Ti6Al4V and Ti6Al4V+B pre-alloyed particles together. Powder satellites and trapped argon porosity were also observed in relatively low concentrations ($< 2\%$) (Figure 3.10d).

Table 3.4. Pre-alloyed and blended powder size analysis, d50 in μm .

| Pre-alloyed Powder | Size d50 (μm) | Blended Powder | Size d50 (μm) |
|--------------------|----------------------------|----------------|----------------------------|
| Ti6Al4V | 110.1 | Ti6Al4V | 110.1 |
| Ti6Al4V+0.25 B | 115.2 | Ti6Al4V+0.10 B | 108.4 |
| Ti6Al4V+0.50 B | 133.5 | Ti6Al4V+0.20 B | 105.9 |
| Ti6Al4V+1.00 B | 104.1 | Ti6Al4V+0.30 B | 109.3 |

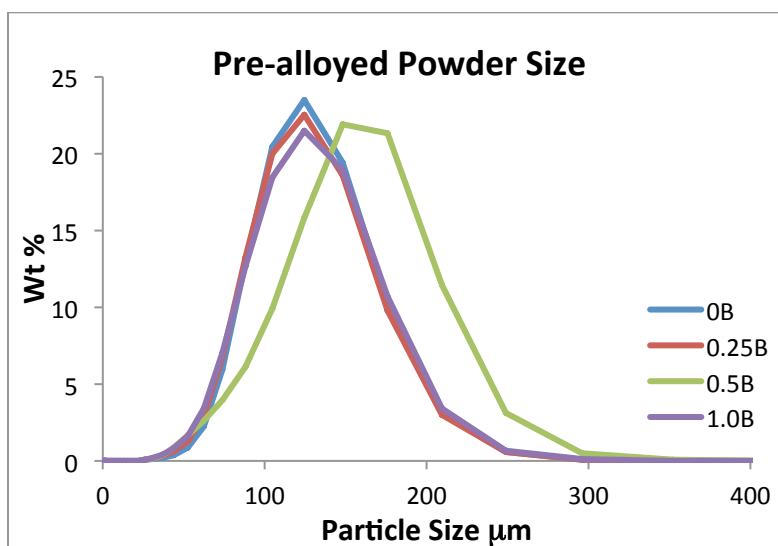


Figure 3.8. Pre-build powder size distribution for Ti6Al4V+B pre-alloyed batches.

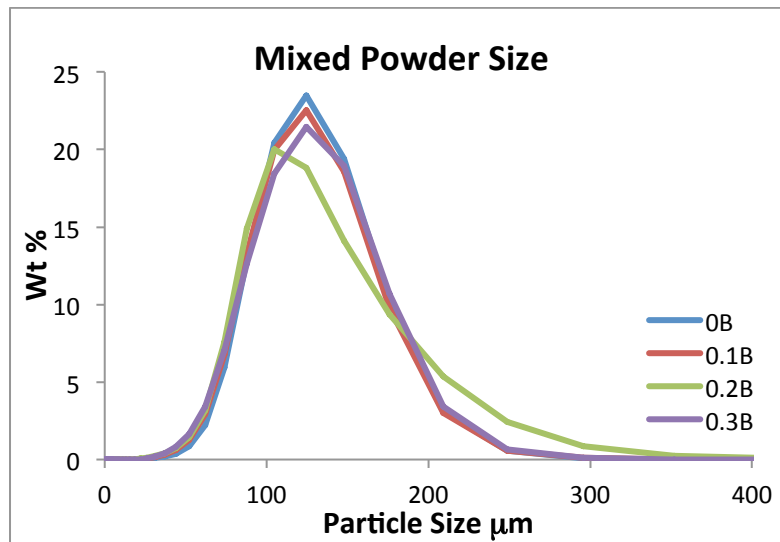


Figure 3.9. Pre-build powder size distribution for Ti6Al4V+B blended batches.

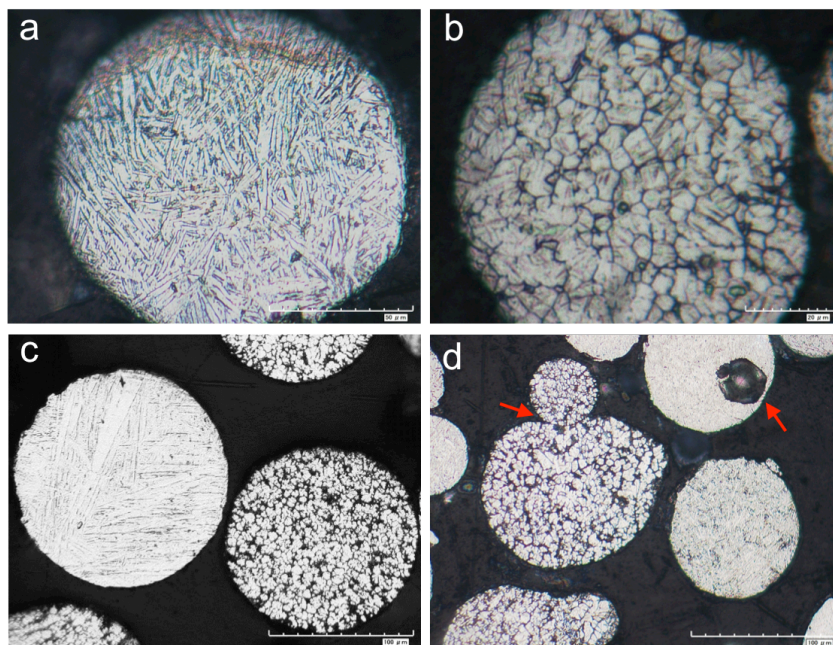


Figure 3.10. a) Ti6Al4V powder particle, b) Ti6Al4V+1.0B powder particle, c) Ti6Al4V+0.3B powder particles, and d) powder defects.

3.2.2. Metallography

Figures 3.11 and 3.12 show digitally reconstructed optical images (using the Hirox tiling function) of Ti6Al4V and Ti6Al4V+B used for grain width measurements; numerical results are reported in Table 3.5. In samples with low boron content, most if not all β grains extended past the viewed area, so β length measurements were not recorded.

In EBM Ti6Al4V, coarse columnar prior β grain boundaries spanning multiple millimeters along the build direction were viewed. The pre-alloyed boron addition of 0.25wt% did not appear to have an effect on grain length; however, β width decreased by 44%. At Ti6Al4V+0.5B, β length appears to reduce. Prior β grain boundaries were not apparent in optical images of Ti6Al4V+1.0B; however, horizontal stratifications roughly equivalent to the layer spacing were observed.

For the blended powders, a decrease in prior β boundary length was measured with increasing additions of Ti6Al4V+1B to Ti6Al4V. As the concentration of Ti6Al4V+1B powder was increased, prior β boundary length correspondingly decreased. Boron additions decreased prior β grain boundary width as compared to the Ti6Al4V control, but no difference in prior β grain width was observed between varying concentrations of blended powders with boron additions. However, Ti6Al4V+B blended samples had grain width values less than Ti6Al4V in all instances.

Table 3.5. Average grain width, in μm , measured from optical micrographs for pre-alloyed and blended Ti6Al4V+B.

| Pre-Alloyed | Grain Width | Blended | Grain Width |
|---------------|-------------|---------------|-------------|
| Ti6Al4V | 88 \pm 51 | Ti6Al4V | 88 \pm 51 |
| Ti6Al4V+0.25B | 49 \pm 25 | Ti6Al4V+0.10B | 48 \pm 23 |
| Ti6Al4V+0.5B | 33 \pm 15 | Ti6Al4V+0.20B | 64 \pm 27 |
| Ti6Al4V+1.0B | -- | Ti6Al4V+0.30B | 50 \pm 24 |

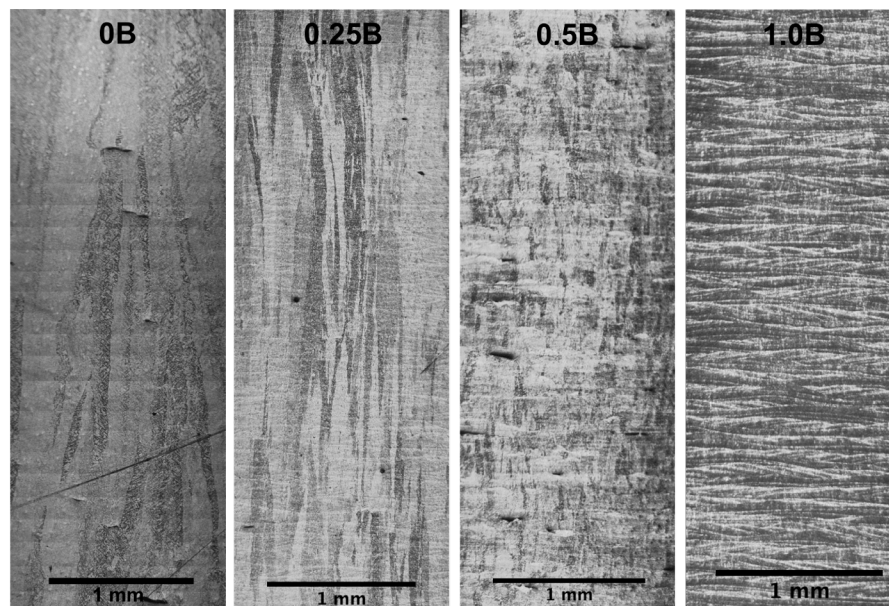


Figure 3.11. Grain structure in Ti6Al4V and pre-alloyed Ti6Al4V+0.25B, Ti6Al4V+0.5B and Ti6Al4V+1.0B EBM samples.

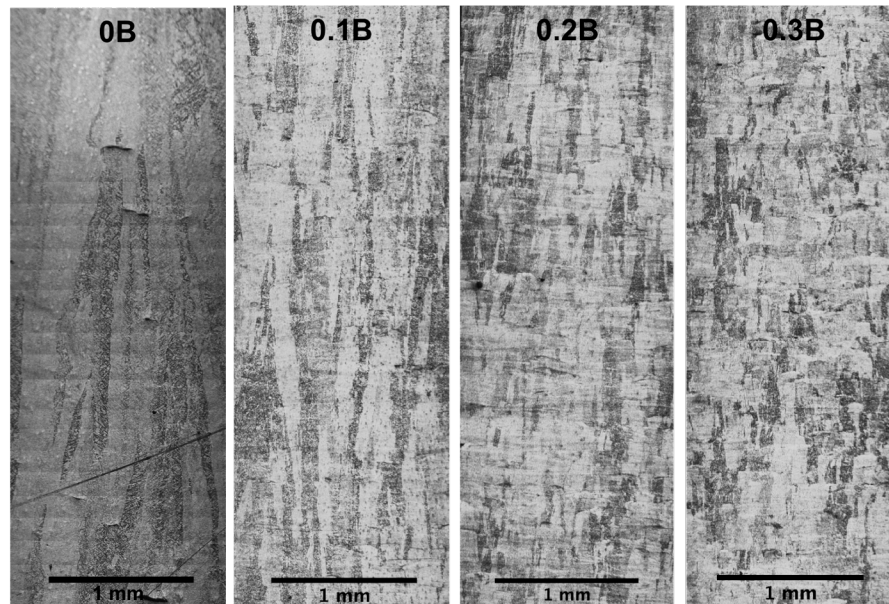


Figure 3.12. Grain structure in Ti6Al4V and blended Ti6Al4V+0.1B, Ti6Al4V+0.2B and Ti6Al4V+0.3B EBM samples.

3.2.3. EBSD

Euler maps for Ti6Al4V and Ti6Al4V+B are shown in Figures 3.13 and 3.14. Average α size is reported for pre-alloyed and blended samples in Tables 3.6 and 3.7, respectively. In the pre-alloyed samples, average grain area was 70% less than the control sample for a 0.25wt boron addition. As expected, α grain size decreases as boron concentration increases for Ti6Al4V+B samples. In the Ti6Al4V+0.25B pre-alloyed sample, average grain area was 70% less than the control sample. Grain area reduction was accompanied by a transition from elongated α laths to a more refined and equiaxed grain morphology. Grain size increases slightly from 0.25wt% to 0.50wt% boron, but then continues to decrease at 1.0wt% boron. Variation in average grain size with boron concentration is plotted in Figures

3.15 and 3.16. After the initial addition of boron, grain size is fairly stable. The number of grains in each EBSD map increased with boron addition. Furthermore, standard deviation decreases linearly with increased boron content.

Average grain size decreased from $9.4\mu\text{m}$ to $2.2\mu\text{m}$ in the Ti6Al4V+0.1 blended boron sample, a 77% reduction. After initial boron addition, grain size increases slightly with additions of 0.2wt% and 0.3wt%, likely due to the increase in the coarse grain boundary α phase with reduced β size. Despite small increase in α size, the number of grains within $220\times 220\mu\text{m}$ increases with each blended boron addition.

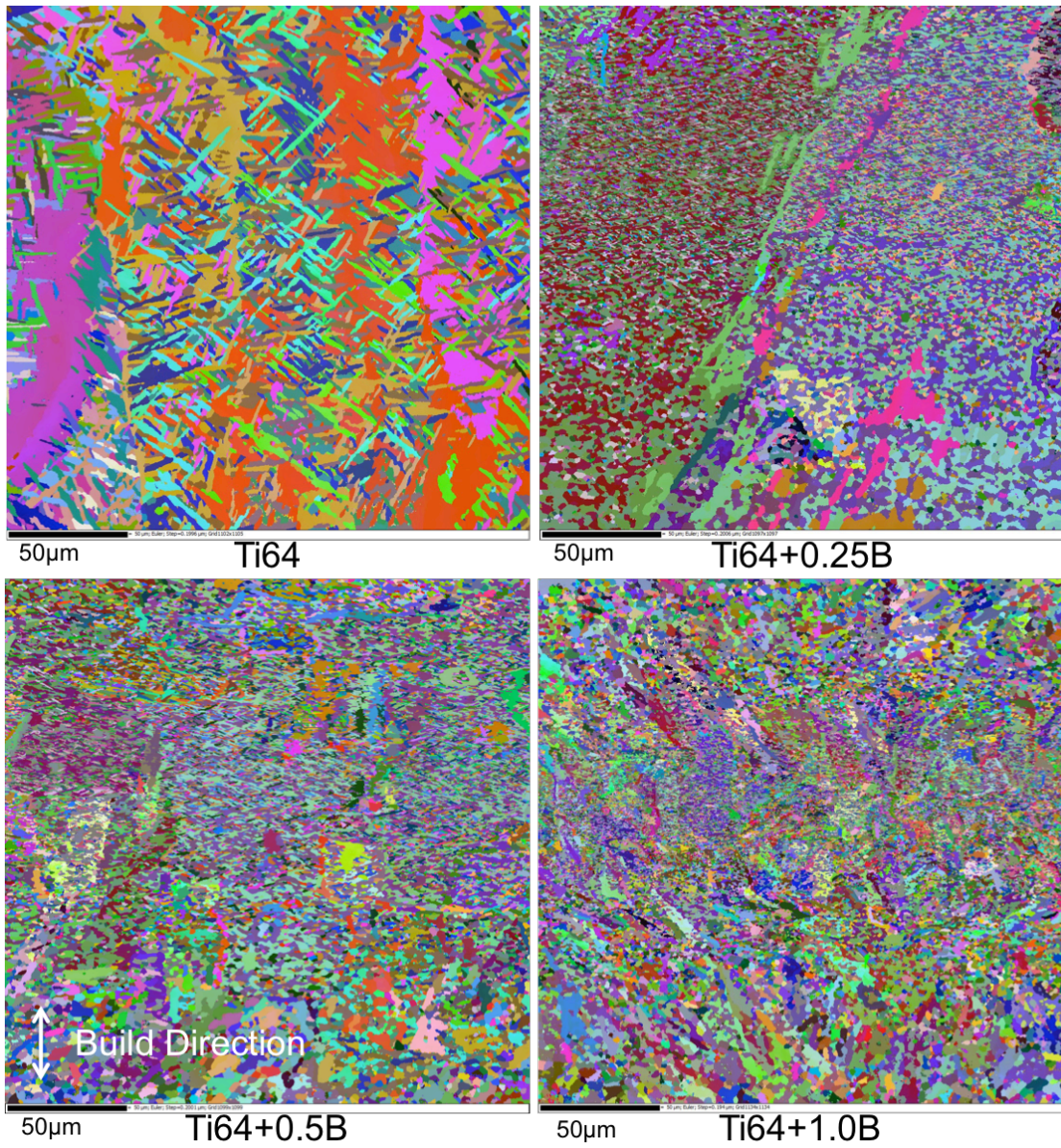


Figure 3.13. 220x220μm EBSD maps of Ti6Al4V and pre-alloyed Ti6Al4V+B with the Euler coloring.

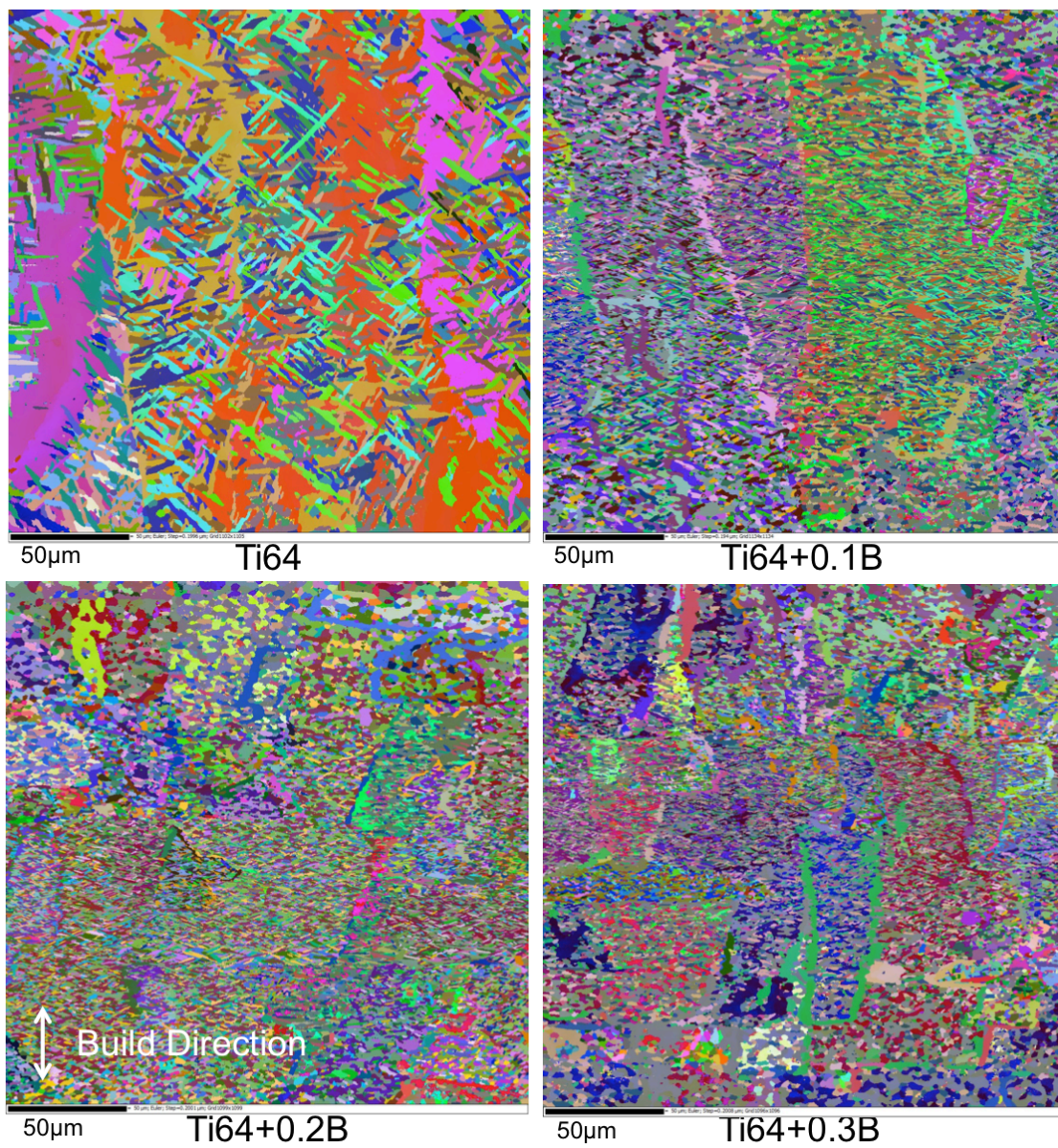


Figure 3.14. 220x220μm EBSD maps of Ti6Al4V and blended Ti6Al4V+B with the Euler coloring.

Table 3.6. Average grain size (μm^2) measured from the bulk of pre-alloyed Ti6Al4V+B microscopy bars. Standard deviation, minimum grain size, maximum grain size, grain count and the 95% confidence interval are reported.

| Pre-alloyed | Ti6Al4V0B | Ti6Al4V0.25B | Ti6Al4V0.5B | Ti6Al4V1.0B |
|---|------------------|---------------------|--------------------|--------------------|
| Average (μm^2) | 9.4 | 2.8 | 3.0 | 2.3 |
| Standard Dev. (μm^2) | 23.0 | 9.6 | 7.5 | 5.3 |
| X_{\min} (μm^2) | 0.4 | 0.4 | 0.4 | 0.4 |
| X_{\max} (μm^2) | 527.4 | 365.0 | 329.4 | 183.1 |
| # Grains | 3609 | 14123 | 14598 | 18275 |
| 95% CI (μm^2) | 0.75 | 0.16 | 0.12 | 0.08 |

Table 3.7. Average α grain size (μm^2) measured from the bulk of blended Ti6Al4V+B microscopy bars. Standard deviation, minimum grain size, maximum grain size, grain count and the 95% confidence interval are reported.

| Blended | Ti6Al4V0B | Ti6Al4V0.10B | Ti6Al4V0.20B | Ti6Al4V0.30B |
|---|------------------|---------------------|---------------------|---------------------|
| Average (μm^2) | 9.4 | 2.2 | 2.7 | 2.9 |
| Standard Dev. (μm^2) | 23.0 | 4.0 | 7.5 | 15.2 |
| X_{\min} (μm^2) | 0.4 | 0.4 | 0.4 | 0.4032 |
| X_{\max} (μm^2) | 527.4 | 115.8 | 462.4 | 1505.3 |
| # Grains | 3609 | 15861 | 16171 | 17643 |
| 95% CI (μm^2) | 0.75 | 0.06 | 0.12 | 0.22 |

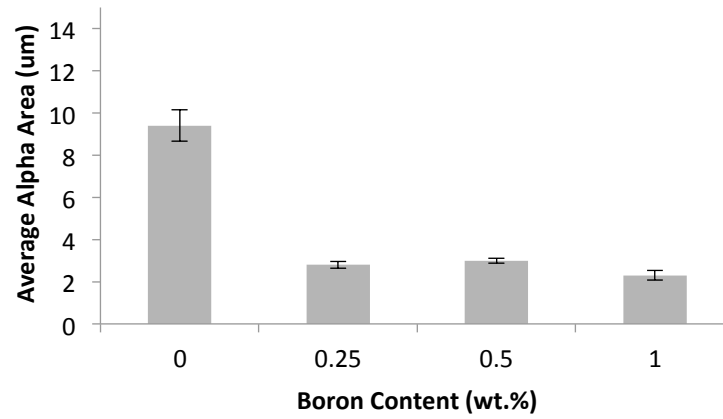


Figure 3.15. Displays average α grain size in μm^2 as a function of pre-alloyed boron content (95% confidence interval).

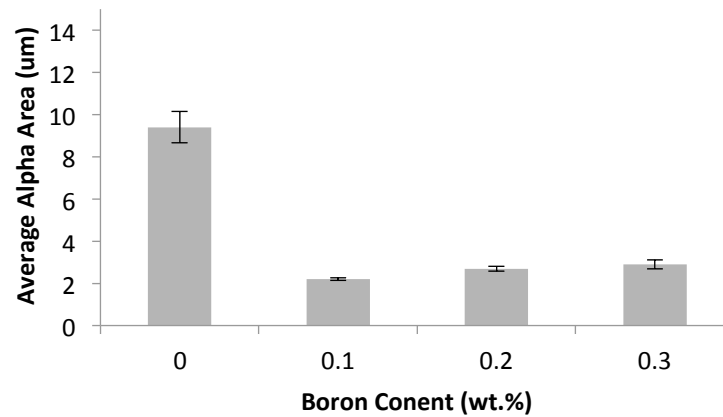


Figure 3.16. Displays average α grain size in μm^2 as a function of blended boron content (95% confidence interval).

3.2.4. X-Ray Diffraction

X-ray spectra for pre-alloyed and blended Ti6Al4V+B solid samples are reported in Figures 3.17 and 3.18, respectively. All spectra show the ten characteristic peaks found in the Joint Committee on Powder Diffraction Standards (JCPDS) reference card for titanium. No significant shift of peak maxima along 2θ was found. There is however an increase in peak intensity for the 35° peak from Ti6Al4V to Ti6Al4V+B. Furthermore, with the addition of boron, a small peak around 42° begins to evolve, it can be seen most prominently in samples with boron additions greater than 0.3wt% as seen in Figure 3.19. This peak could correspond to the 42.6° peak in the TiB JCPDS. JCPDS peak data are reported in the Appendix.

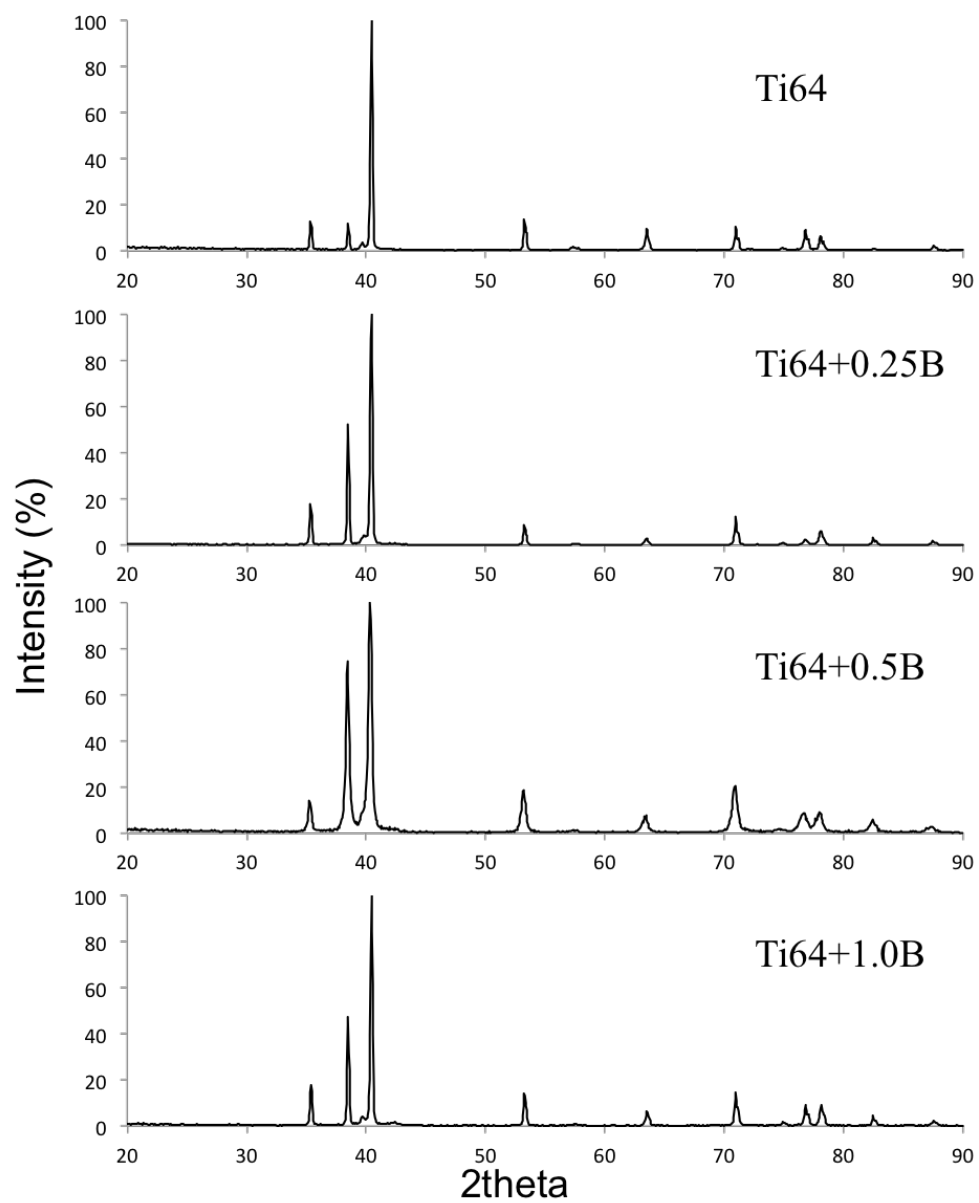


Figure 3.17. XRD spectra for Ti6Al4V and pre-alloyed Ti6Al4V+B samples.

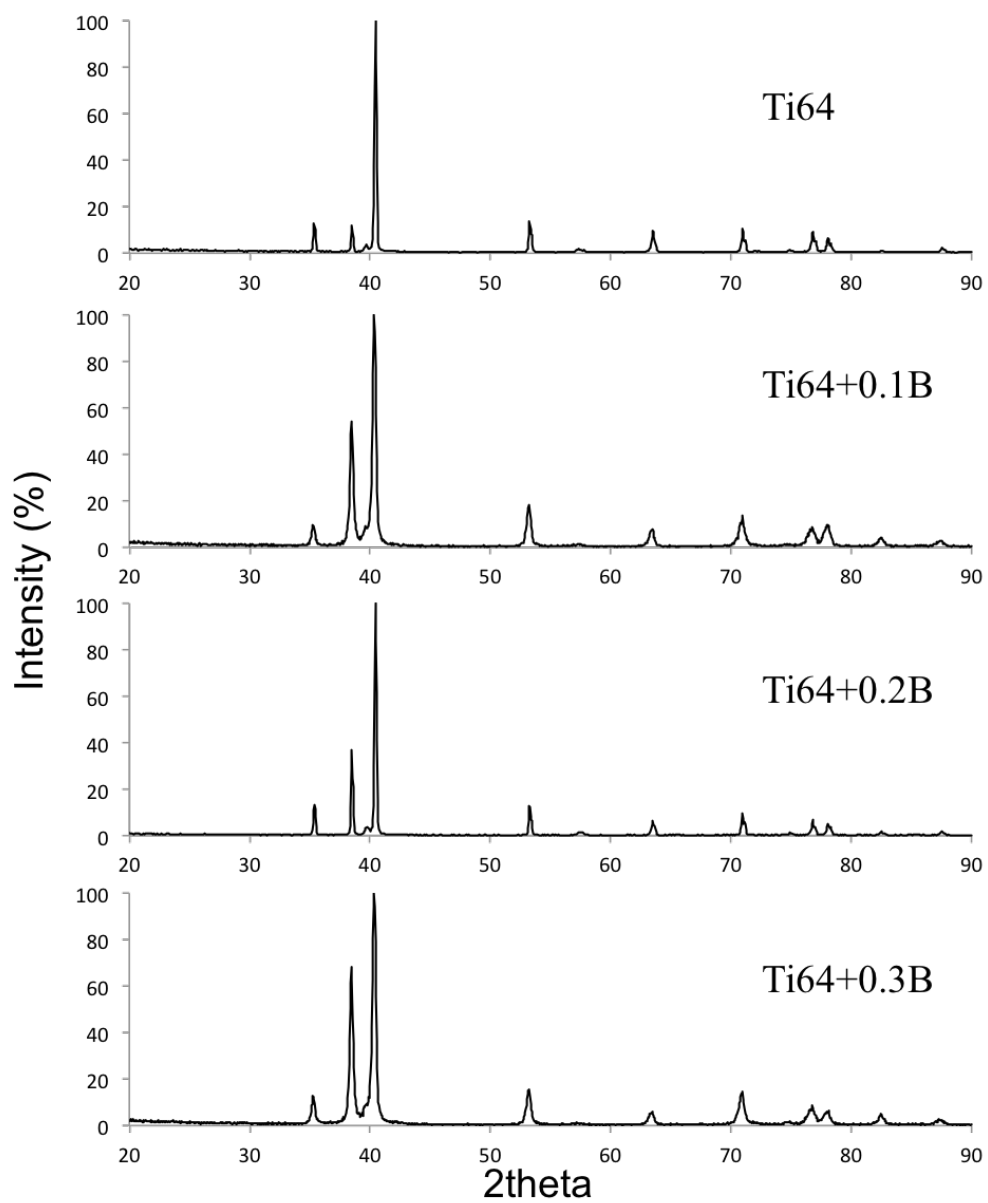


Figure 3.18. XRD spectra for Ti6Al4V and blended Ti6Al4V+B samples.

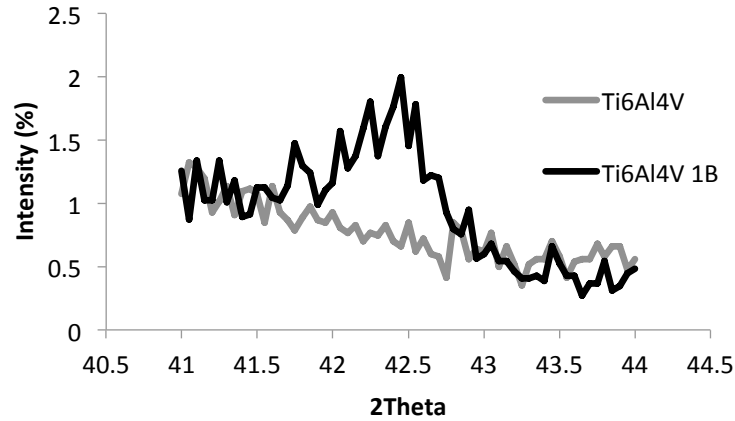


Figure 3.19. Development of TiB peak at 42.6deg in Ti6Al4V+B.

3.2.5. Electron Microscopy

The TiB phase, evident in Ti6Al4V castings at the prior β grain boundaries [Roy, 2011] was not observed in the EBM processed samples with BSE-SEM analysis; instead dark regions $<1\mu\text{m}$ were imaged within the microstructure of all EBM Ti6Al4V+B samples. Backscatter electron images of Ti6Al4V and Ti6Al4V+B are depicted in Figures 3.20 and 3.21. EDS was performed on all BSE images, and detected elements (Ti, Al, V, N) were all homogeneously distributed. In particular, dark regions did not contain a more dense distribution of nitrogen or aluminum to explain their color in relation to the gray matrix.

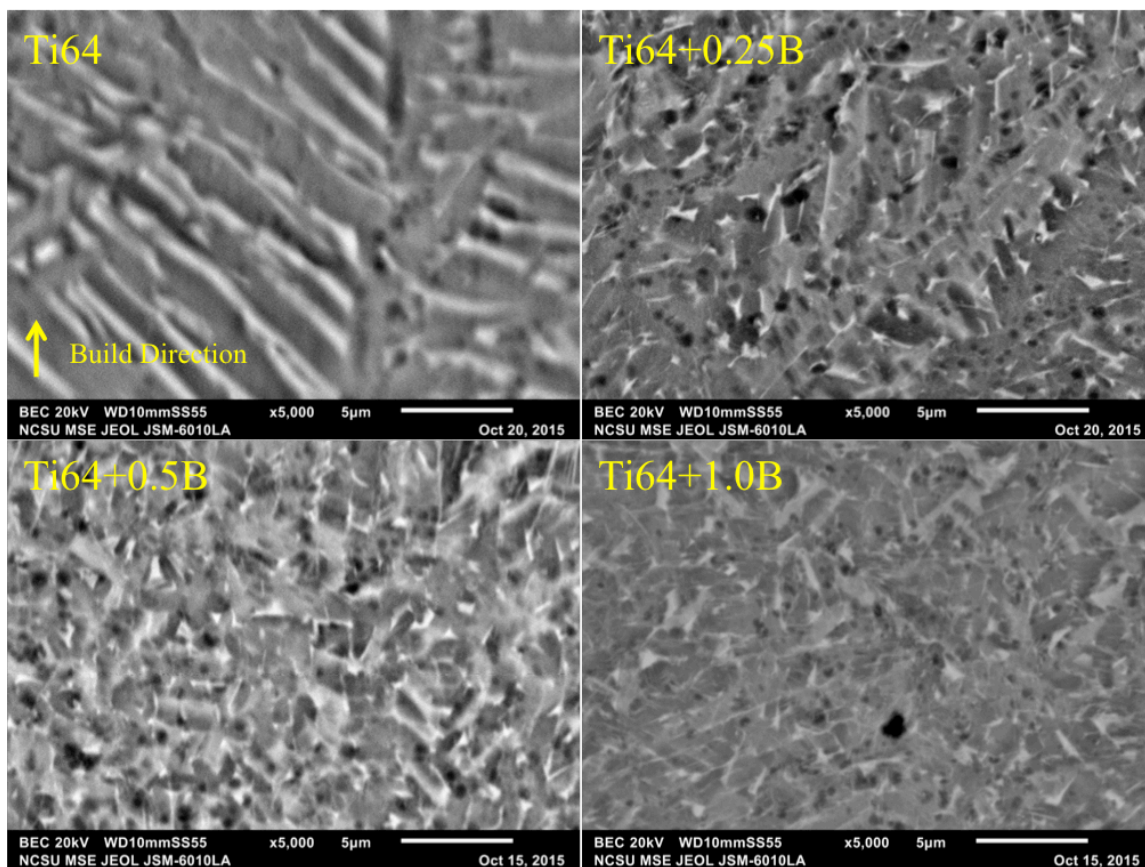


Figure 3.20. BSE images of Ti6Al4V and pre-alloyed Ti6Al4V+B. Dark areas $<1\mu\text{m}$ were imaged in all samples with boron addition.

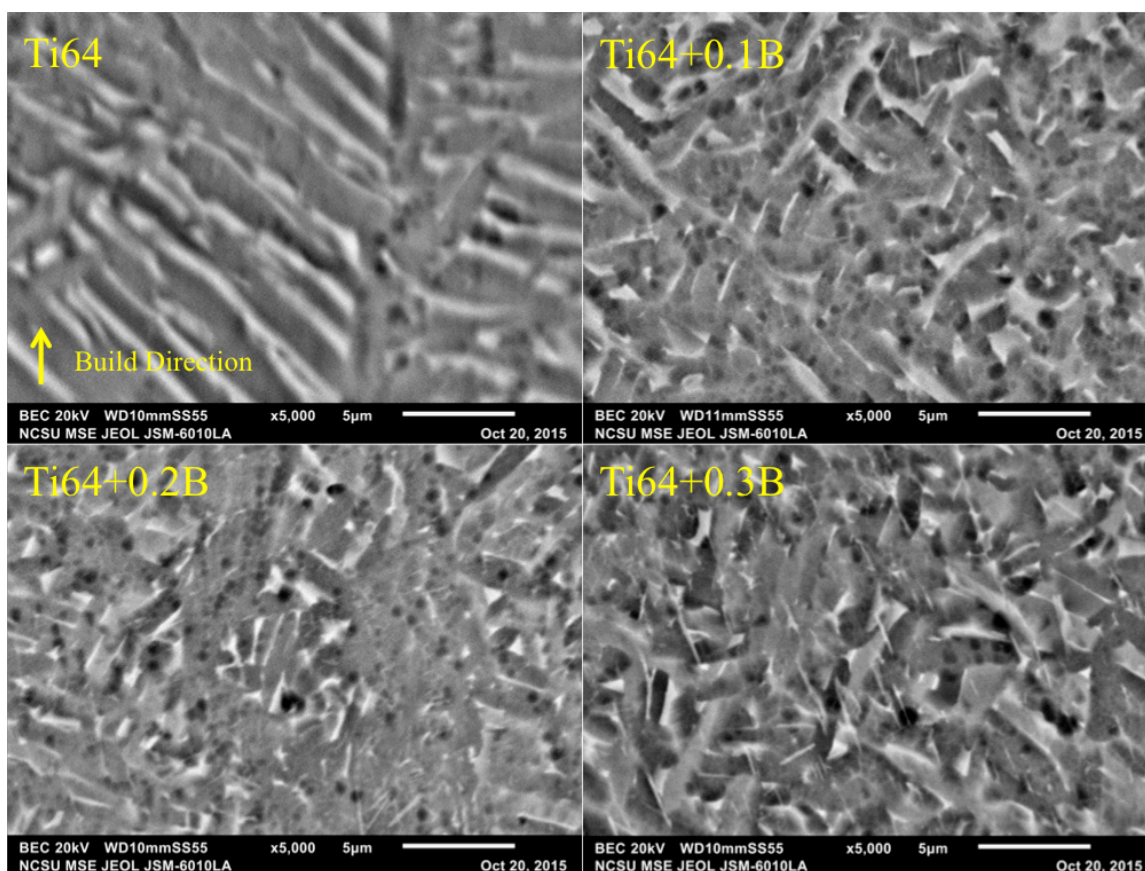


Figure 3.21. BSE images of Ti6Al4V and blended Ti6Al4V+B. Dark regions $<1\mu\text{m}$ were imaged in all samples with boron addition.

3.2.6. Chemistry

Elemental concentrations in pre-alloyed and blended Ti6Al4V+B samples are reported in Table 3.8. ICP data indicates that all samples have Al, V and Fe concentrations within the acceptable range for Ti6Al4V as defined by ASTM B348 (reported in the “Estimated” row). Projected boron concentration for the pre-alloyed samples was 0, 0.25, 0.50 and 1.0wt%; measured boron concentrations were <0.01 , 0.27, 0.39 and 1.06wt%. Concentrations range from 0.02-0.11wt% from the expected values. ICP results for blended samples, containing

Ti6Al4V+1.0B with different dilutions of Ti6Al4V, closely matched the predicted values (only varying by ≤ 0.01 wt%). Combustion elemental analysis gives the weight percent of the C, O and N impurities in Ti6Al4V to 10ppm. Like the ICP-mass spectrometry data, all values are below the acceptable amount for Ti6Al4V per ASTM B348.

Table 3.8. ICP and combustion chemical analysis data for blended and pre-alloyed Ti6Al4V+B samples.

| Alloy | Al | V | B | Fe | C | O | N |
|------------------|-----------------|----------------|--------------|----------------|-----------------|----------------|-----------------|
| Estimated | 5.5-6.75 | 3.5-4.5 | 0-1.0 | <0.4 | <0.08 | <0.2 | <0.05 |
| Ti6Al4V | 5.85 | 4.10 | <0.01 | 0.11 | 0.02 | 0.16 | 0.01 |
| Ti6Al4V0.25B | 5.62 | 4.14 | 0.27 | 0.08 | 0.05 | 0.11 | 0.02 |
| Ti6Al4V0.50B | 5.68 | 4.18 | 0.39 | 0.16 | 0.05 | 0.15 | 0.01 |
| Ti6Al4V1.00B | 5.71 | 4.14 | 1.06 | 0.20 | 0.06 | 0.15 | 0.04 |
| Ti6Al4V0.10B | 5.86 | 4.07 | 0.11 | 0.12 | 0.03 | 0.17 | 0.01 |
| Ti6Al4V0.20B | 5.78 | 4.05 | 0.21 | 0.23 | 0.03 | 0.17 | 0.02 |
| Ti6Al4V0.30B | 5.89 | 4.06 | 0.30 | 0.14 | 0.03 | 0.17 | 0.02 |

3.3. Discussion

3.3.1. Powder Analysis

Gas atomization (GA) is a common method used to produce high quality metal powders for EBM. In GA, liquid metal is atomized with gas jets, and the droplets freeze in controlled atmosphere. Powders produced with this method typically have smooth surfaces and a spherical morphology, providing ideal flow characteristics for EBM [Dunkley, 1998].

GA powders often contain particles with internal voids, as shown in Figure 3.10; these originate from the entrapment of gas during atomization. In addition, some powder satellites,

finer particles attached to coarser particles, were observed in the powders. Circulation of gas within the atomization chamber can lift finer particles causing collisions with larger particles that are not fully solidified leading to the formation of satellite morphologies [Dunkley, 1998]. Satellites can break off during powder handling (sieving, blending, etc.), and decrease the minimum particle size of a distribution. Smaller particles have greater surface area and lower gravitational forces acting up on them; therefore, can more easily cause a “smoke” event during EBM. Powder “smoking” occurs during the EBM process when the electron beam charges the powder bed. If electrical conduction between the powder and ground is insufficient, the charge increases until the repulsive forces between powder particles overcome gravitational forces and creates a powder cloud inside the chamber [Karlsson, 2015]. Both gas entrapment and satellites are common occurrences in GA powders. Trapped gas inside powder particles can, under the right conditions, manifest as spherical pores in an EBM fabricated part.

Despite high cooling rates in GA, the pure Ti6Al4V powder particles contained the characteristic Widmanstätten microstructure. A more refined microstructure exists in the powder particles containing boron. Boron addition disrupts the growth of long α laths; instead, a refined structure is developed. Each powder batch was projected to have a Gaussian distribution containing particle size ranging from 45-105 μm with a median diameter $d_{50}=80\mu\text{m}$. Pre-alloyed powder size was about 10 μm higher than expected (excluding Ti6Al4V+0.5). Ti6Al4V+0.5B powder had median diameter $d_{50}=133\mu\text{m}$. Large

discrepancies in powder size may require adjusting processing parameters, which were optimized for 100 μm Ti6Al4V; however, in this study, the same processing parameter set was used for all samples.

3.3.2. Microstructural Analysis

3.3.2.1. Ti6Al4V

Metallographic and EBSD analyses of EBM fabricated Ti6Al4V show columnar prior β grain boundaries, and α laths with a high aspect ratio. During solidification of Ti6Al4V, β grains nucleate and grow in the liquid melt. After the temperature decreases below the β transus, the grain boundary α phase nucleates heterogeneously on the β grains [Al-Bermani, 2010]. Widmanstätten α platelets are formed and rod-shaped β phase nucleates on the interface of these platelets. In the bulk of a layer in EBM, heat cannot be readily transferred into the surroundings; instead, it is ejected into previously solidified layers. The reheating of layers promotes the continuous growth of grains that span several layers along the build axis.

3.3.2.2. Ti6Al4V with Pre-alloyed Boron

In literature regarding castings, the microstructures of Ti6Al4V and Ti6Al4V+B were characterized by alternating α and β lamellae within prior β grain boundaries. The presence of the TiB phase at prior β grain boundaries was unique to the Ti6Al4V+B alloys [Luan, 2014; Luan, 2015; Roy, 2011; Sen, 2007; Sen, 2010; Sen and Ramamurty, 2010; Tamirisakandala, 2005; Zhu, 2003]. In all instances, the grain boundary α phase was absent

in areas where TiB had precipitated. The volume fraction of TiB exceeded that of the grain boundary α phase in Ti6Al4V+0.1B castings [Roy, 2011]. Despite similarities in microstructure, α and β grain size was reduced by an order of magnitude with only 0.1wt% boron addition [Roy 2011; Sen, 2007; Tamirisakandala, 2005].

Roy et al. has described this mechanism in castings. Based on the Ti-B phase diagram, boron has negligible solubility in solid titanium ($<0.02\text{wt}\%$) [2011]. During the solidification of alloys, a solute element with low solid solubility will be ejected ahead of the solid/liquid interface during the growth of a crystal. A solute concentration gradient (X_L) exists ahead of the solidification front giving rise to a variation in liquidus temperature. The temperature of the liquid melt ahead of the growing crystal (T_L) varies depending on the solute concentration. If T_L is below the equilibrium solidification temperature (T_e), then the liquid is supercooled as a result of compositional effects. This is called constitutional (compositional) supercooling and is illustrated in Figure 3.22 [Callister, 2014].

During the solidification of cast Ti6Al4V+B, β grains nucleate and grow below the liquidus temperature (Figure 3.23). Boron is rejected from β crystals creating a solute rich liquid trapped between β grains; this liquid solidifies as TiB below the eutectic temperature. Further cooling below the β transus triggers the β to α transformation. Boron enrichment ahead of the solidification front produces a variation in liquidus temperature leading to high degrees of constitutional supercooling. Constitutional supercooling provides an additional

driving force for the nucleation of β grains in the remaining liquid. Furthermore, the boron rich liquid layer retards the growth of grains allowing nucleation of more β grains in the supercooled melt. Final grain size is determined by the competition between nucleation and growth. Increased nucleation and decreased growth as a result of constitutional undercooling produced a fine and equiaxed grain structure in Ti6Al4V+B castings [Roy, 2011].

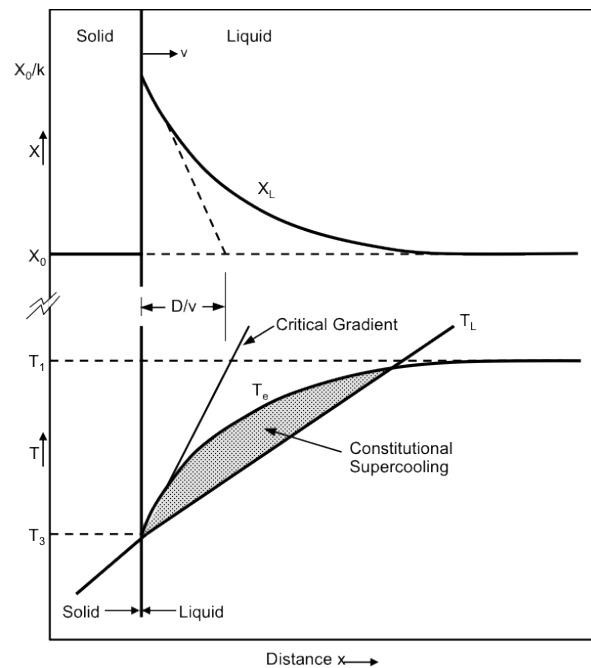


Figure 3.22. Constitutional supercooling takes place when liquid temperature (T_L) is lower than equilibrium solidification temperature (T_e). Changes in solidification temperature are caused by differences in solute concentration (X_L). Recreated from Callister, 2014.

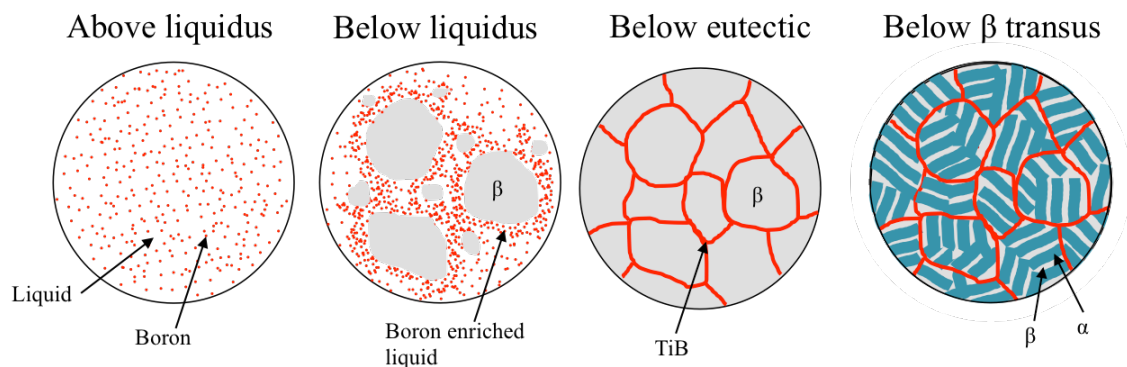


Figure 3.23. Microstructural evolution of Ti6Al4V+B in castings.

The slow cooling rate in castings allow for adequate growth of α/β crystals and complete boron diffusion to grain boundaries. In EBM, high cooling rates on the order of 10^3 - 10^5 K/s [Al-Bermani, 2010], and the layer-by-layer solidification process differ fundamentally from solidification in castings. Literature concerning laser and electron beam processing of materials asserts that during rapid solidification several assumptions of the constitutional supercooling criterion might not be valid. (1) Surface tension and latent heat evolution which could stabilize the solid/liquid interface are neglected. (2) The constitutional supercooling theory specifies a layer of liquid cooler than its melting point, but does not describe how the crystal breaks through this layer. (3) Local equilibrium at the interface is presumed to give the amount of solute rejected from the growing crystal [Kimmitt, 1981]. During rapid solidification, constitutional supercooling may incorrectly predict the solid/liquid instability behavior. The grain refinement mechanism in EBM Ti6Al4V+B will be predicted from microstructural, chemical and XRD analysis.

BSE images of EBM Ti6Al4V reveal elongated α crystals within prior β grain boundaries. The bright and gray areas demarcate the β and α crystals, respectively. Boron addition at every concentration disrupts the α/β lath structure such that no directional solidification of crystal exists; instead, refined and equiaxed features are observed. EBSD orientation maps assert that after any addition of boron there is no alignment of the α phase; α grows randomly within the β matrix. Optical analysis of the pre-alloyed powders also demonstrates the non-directional solidification of grains in Ti6Al4V+B.

Chemical analysis validates that elemental boron is present in the material after EBM fabrication. XRD spectra for Ti6Al4V and Ti6Al4V+B fit the JCPDS card for elemental titanium. A low intensity $\sim 2\%$ peak near 42.6deg was unique to the Ti6Al4V+B spectra. In the TiB spectrum, there is a characteristic 100% intensity peak at 42.6 degrees. The intensity of this peak is greatly reduced in Ti6Al4V+B samples due to the low concentration of TiB within the final microstructure. Another difference between Ti6Al4V and Ti6Al4V+B is the presence of dark circular features $< 1\mu\text{m}$ in BSE micrographs of Ti6Al4V+B. EDS analysis did not show a higher distribution of nitrogen or aluminum in these areas. It is possible that the dark spots are the TiB phase homogeneously distributed throughout the matrix. Alternatively, the TiB phase might be undetectable without transmission electron microscopy analysis. Regardless, chemical and XRD data prove that the TiB phase is present within the final microstructure of EBM Ti6Al4V+B. BSE and EBSD analysis show that the presence of boron greatly alters the solidification of Ti6Al4V at all concentrations.

Based on optical, BSE, EBSD, XRD and chemical analyses, the microstructural evolution of EBM Ti6Al4V+B is predicted. Above the liquidus temperature, boron is homogeneously distributed in molten Ti6Al4V (Figure 3.24). Upon cooling below the liquidus, the boron acts as heterogeneous nucleation sites for β grains. High cooling rates and the dense distribution of nucleation sites leads to the simultaneous nucleation of β throughout the entire liquid matrix. The microstructure now contains a random mix of equiaxed β particles. The boron, unable to diffuse from rapidly solidifying β grains, precipitates as TiB below the eutectic temperature. Final cooling below the β transus promotes α nucleation on the TiB precipitates. Distinct prior β grain boundaries are not observed in microstructural analysis due to the absence of the grain boundary α and TiB phases at the prior β grain boundaries of Ti6Al4V+0.5 and Ti6Al4V+1.0B. Grain size is reduced and homogenized because nucleation rate is greatly favored over growth. During the melting of subsequent layers, grains do not grow along the build direction because the preferred nucleation sites are still distributed throughout the matrix allowing for re-nucleation of β .

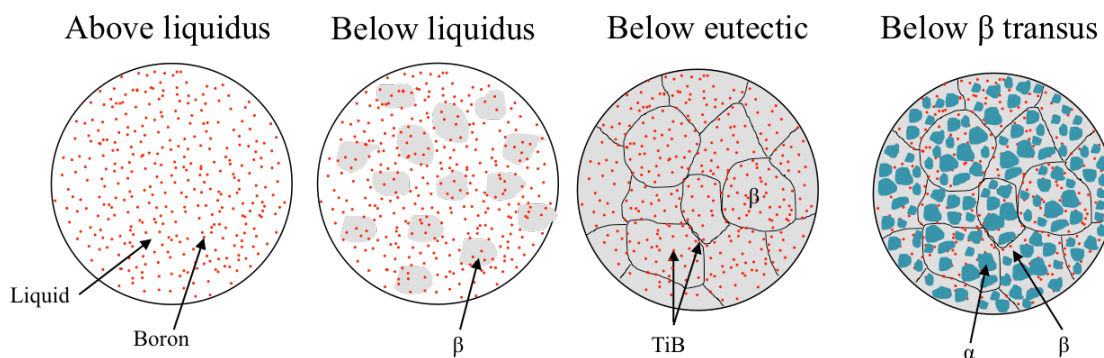


Figure 3.24. Predicted microstructural evolution of a single layer in EBM fabricated Ti6Al4V+B.

3.3.2.3. *Ti6Al4V with Blended Boron*

Defined prior β grain boundaries are visible in optical and EBSD micrographs of samples built from Ti6Al4V blended with Ti6Al4V+1.0B powders. Additionally, a large volume of the grain boundary α phase is present at prior β boundaries. In pre-alloyed samples, both β and α grain widths decrease with the addition of boron; however, no relationship between boron concentration and β width was measured in blended Ti6Al4V+B. Alpha widths were not measured, but they appear to be elongated along the XY plane in the EBSD orientation maps. The blended boron microstructures more closely resemble an equilibrium microstructure than pre-alloyed samples, so a different solidification mechanism is likely occurring.

Blended powder samples contain mostly pure Ti6Al4V powder, so the solidification of pure Ti6Al4V should be considered. During solidification, β nucleates and grows opposite the direction of heat flow. Below the β transus, the α crystals nucleate and grow within the prior β grains. Stochastically, a powder particle containing boron will be spread within a single layer; its presence will increase β/α nucleation locally as it did in pre-alloyed batches. As blended boron concentration increases there are a greater number of particles containing boron in the powder, so the probability of a pre-alloyed particle existing in an area is increased.

3.3.3. Chemistry

Boron concentration in the pre-alloyed powders was close to the intended values with the exception of the Ti6Al4V+0.5 powder batch. Although the Ti6Al4V+0.5 powder had boron concentration closer to 0.4wt%, data collected can still be used to evaluate microstructural changes between 0.25 and 1.0wt% boron additions.

Elemental analysis verifies that boron exists in the material after the electron beam melting process. However, because powder chemistry was not tested before EBM fabrication it is not known if any evaporation of elemental boron occurred. Furthermore, chemical analysis validated the effectiveness of the powder blending technique in creating homogeneous blends of pure Ti6Al4V and pre-alloyed powders.

3.4. Conclusion

The addition of boron to EBM Ti6Al4V in pre-alloyed (0.25, 0.50 and 1.0wt%) and blended (0.10, 0.20 and 0.30wt%) concentrations drastically refines the β and α grain size. Based on experimental observations, the following conclusions have been drawn:

1. The absence of TiB at prior β boundaries in EBM Ti6Al4V+B suggests that a grain refinement mechanism other than constitutional supercooling might be taking place.

2. Metallographic, BSE and EBSD analyses show that the addition of boron alters the solidification of EBM Ti6Al4V. Most notably, the lack of elongated α crystals in Ti6Al4V+B was observed.
3. Chemical and XRD data suggest that the TiB phase exists within in the final microstructure

CHAPTER 4: MECHANICAL PROPERTIES OF ELECTRON BEAM MELT FABRICATED Ti6Al4V WITH BORON ADDITION

Grain refinement via hypoeutectic boron additions is well documented for Ti6Al4V castings. In this chapter the effects of boron additions on the mechanical properties of EBM fabricated Ti6Al4V are investigated. The addition of boron is hypothesized to increase the hardness, elastic modulus and tensile strength while reducing ductility of Ti6Al4V. Mechanical properties of pre-alloyed and blended Ti6Al4V+B samples are evaluated using Vickers hardness, flexural and tensile testing.

4.1. Materials and Methodology

4.1.1. Vickers Microhardness

Hardness testing was performed on polished samples following optical metallography. A LECO MHT Series 200 (St. Joseph, MI) micro-indentation hardness tester equipped with a pyramidal diamond indenter was used to test each sample at 1000g for 30 seconds. Indent marks were spaced roughly 3 diagonal lengths apart to ensure that hardness values were not skewed due to the plastic deformation from another measurement. The distance between diagonal corners of each indent mark was measured. Average Vickers hardness (HV) was calculated using the mean diagonal length (d) in μm and Equation 3.

Equation 3:

$$HV = \frac{F}{A} = \frac{1854.4P}{d^2}$$

where P is load in grams.

4.1.2. Flexural Testing

Preliminary tensile testing indicated a brittle failure mechanism for Ti6Al4V+1B samples, therefore four point flexure tests were carried out in order to determine the elastic modulus of the materials used in this study. Flexure specimens fabricated with EBM to 0.98 x 0.31 x 6.50 inches were milled to a final dimension of 0.48 x 0.24 x 6.5 inches using a CNC milling machine (Figure 4.1). Milling was completed on 4 sides of each bar (excluding the ends) with a 2.25 inch diameter carbide insert shell mill, peripheral velocity of 0.6 ft/s and flooding with CimTech 320Z with InSol technology metalworking fluid. Low cutting speeds and ample coolant were used to minimize tool wear that could affect surface finish; these parameters are reported in Table 4.1. After milling, surface roughness was measured along the center of each flexure bar using a stylus profilometer (Mitutoyo SurfTest SJ-210, Aurora, IL). Ten roughness measurements were collected for each sample.

Four point flexure tests were carried out using an Applied Test Systems 1620 universal testing machine (Butler, PA). A photograph of the testing fixture is shown in Figure 4.2. The inner loading pins (0.375 inches in diameter) were spaced 1 inch apart (L_i), and outer support pins (0.75 inches in diameter) were 5.5 inches apart. Six replicates of each of the seven chemistries were loaded at a rate of 0.1 inch per minute. Data was recorded at a rate of 95 Hz with a 5000lb load cell (ATS Series 16200OC Universal Test Machine). An

extensometer (Epsilon 3540-100T ST, Jackson, WY) was placed directly below the center of the specimen to measure displacement. Preliminary tests indicated that the ultimate load in flexure was ~1000 lbs, therefore in order to ensure that flexure tests were inherently non-destructive bars were loaded to 20% of this value, or 200lbs, to obtain a displacement versus load curve to calculate elastic modulus.

Table 4.1. Milling parameters for Ti6Al4V and Ti6Al4V+B flexure bars.

| | |
|-----------------------------------|-------------|
| Spindle speed | 100 RPM |
| Surface speed | 352 IPM |
| Feed rate | 0.50 IPM |
| Maximum Rough Depth of Cut | 0.01 inches |

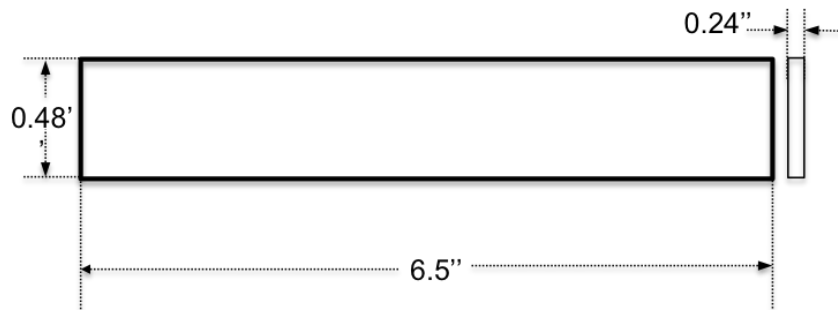


Figure 4.1. Flexure bar sample dimensions after milling.

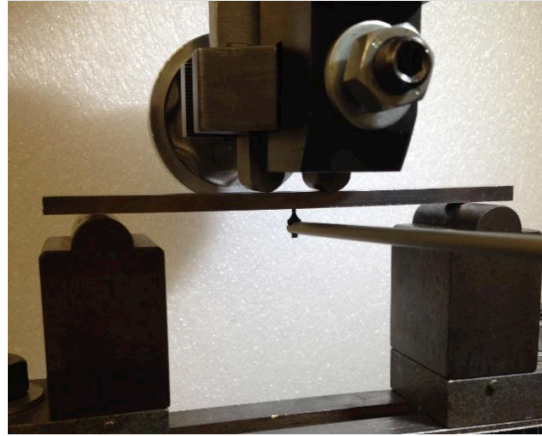


Figure 4.2. Photograph of 4-point bend setup where L_1 is 1in, L is 5.5in and d is 0.24in.

4.1.3. Tensile Testing

After nondestructive flexure testing, the samples were milled into tensile specimens with a 2-inch gage length shown in Figure 4.3 (0.24 x 0.24 inch cross-section). Peripheral milling was completed in the HAAS Tool Room 3-axis mill (Oxnard, CA) with a 0.375 inch carbide mill (29 SFM). The milling set-up is depicted in Figure 4.4. Before testing, machined sample surfaces were imaged using a Hirox KH-7700 (Hackensack, NJ) digital light microscope due to the observation of voids on machined surfaces. Samples were clamped with wedge grips and loaded until failure at a rate of 0.1 inch per minute (Figure 4.5); data was collected at a rate of 95 Hz with a 20,000lb load cell (ATS 1620 Universal Test Machine, Butler, PA). Percent area reduction at the fracture surface was measured with the Hirox KH-7700 (Hackensack, NJ) digital light microscope.

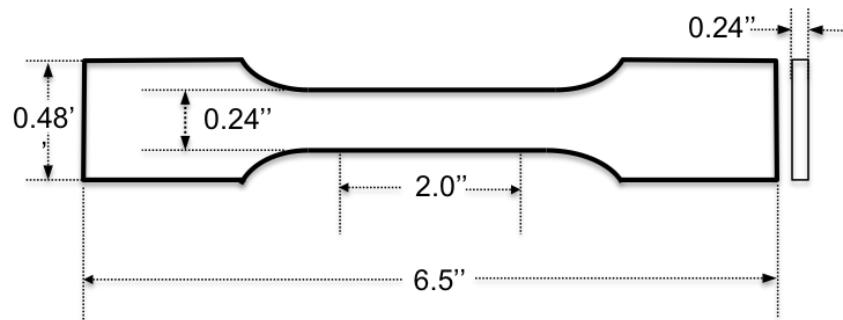


Figure 4.3. Tensile bar sample dimensions after milling.



Figure 4.4. Tool room mill set-up for tensile bar machining.



Figure 4.5. Tensile testing setup.

4.1.4. Electron Microscopy

Fracture surfaces were inspected with a Hitachi S3200N Variable Pressure SEM (Tokyo, Japan). Location of fracture initiation and areas containing pores, voids and un-melted powder particles were imaged in secondary electron mode.

4.2. Results

4.2.1. Mechanical Properties

Hardness, flexural modulus, ultimate tensile strength and percent area reduction are reported in Table 4.2. Figures 4.6-4.9 plot Vickers hardness and percent area reduction versus boron content. Hardness and elastic modulus increase linearly with increasing boron. Percent area reduction closely follows the α/β grain size reduction trends. The Ti6Al4V+1.0B bars exhibited little to no ductility. Furthermore, UTS of all Ti6Al4V+B

samples is lower than that of Ti6Al4V (except the Ti6Al4V+1.0B sample). Samples with 0.50wt% boron showed the greatest reduction in UTS. Tensile modulus ranged from 17100-18100ksi and was consistently higher than flexural modulus (except for Ti6Al4V+1B); however, challenges with gripping the brittle Ti6Al4V+B samples lead to a high variation in the data.

Table 4.2. Vickers hardness, flexural modulus, ultimate tensile stress and percent area reduction data for Ti6Al4V and Ti6Al4V+B with a 95% confidence interval.

| Alloy | Hardness (HV) | Flexure MOE (ksi) | UTS (ksi) | Area Reduction (%) |
|----------------------|----------------------|--------------------------|------------------|---------------------------|
| Ti6Al4V | 324 ± 6 | 16800 ± 88 | 168 ± 2 | 25 ± 4 |
| Ti6Al4V+0.25B | 345 ± 4 | 17300 ± 175 | 152 ± 2 | 8 ± 1 |
| Ti6Al4V+0.50B | 375 ± 13 | 17200 ± 263 | 142 ± 11 | 3 ± 1 |
| Ti6Al4V+1.00B | 422 ± 10 | 18300 ± 175 | 178 ± 1 | 1 ± 0 |
| Ti6Al4V+0.10B | 348 ± 6 | 17000 ± 175 | 148 ± 1 | 15 ± 3 |
| Ti6Al4V+0.20B | 361 ± 5 | 17100 ± 175 | 156 ± 1 | 7 ± 2 |
| Ti6Al4V+0.30B | 365 ± 6 | 17300 ± 88 | 161 ± 1 | 4 ± 0 |

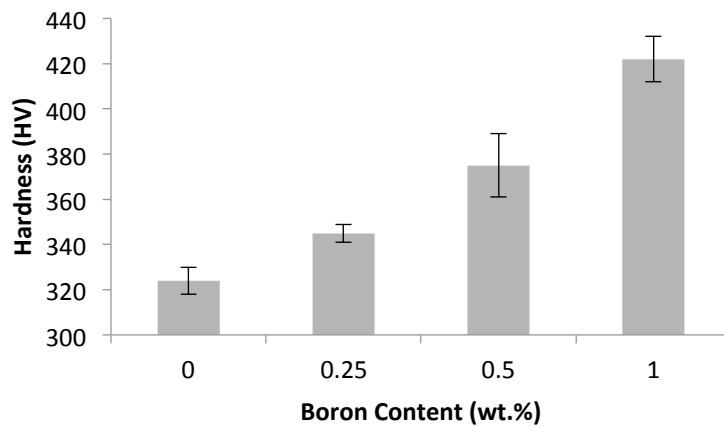


Figure 4.6. Changes in microhardness with pre-alloyed boron content in Ti6Al4V (95% confidence interval).

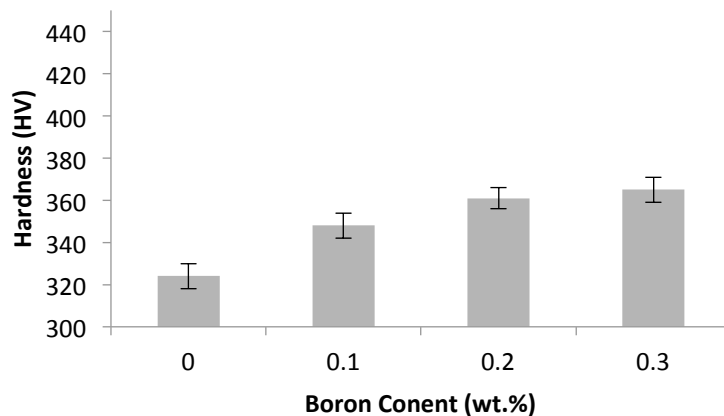


Figure 4.7. Changes in microhardness with blended boron content in Ti6Al4V (95% confidence interval).

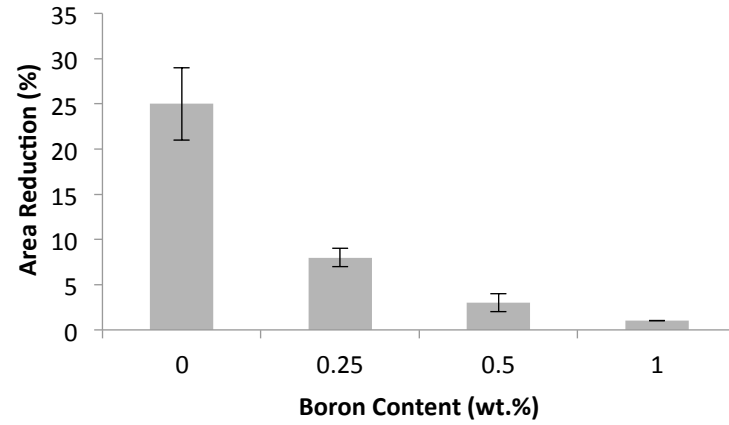


Figure 4.8. Changes in percent area reduction with pre-alloyed boron content in Ti6Al4V (95% confidence interval).

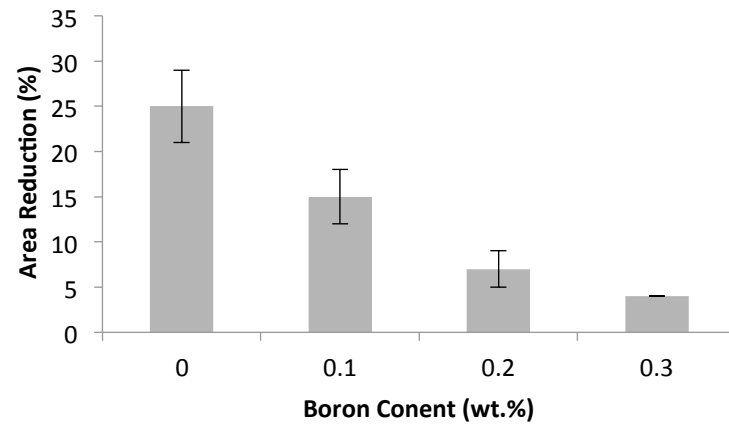


Figure 4.9. Changes in percent area reduction with blended boron content in Ti6Al4V (95% confidence interval).

4.2.2. Optical Microscopy

Tensile machining exposed porosity and delaminating layers in all Ti6Al4V+0.50B tensile specimens (Figure 4.10).

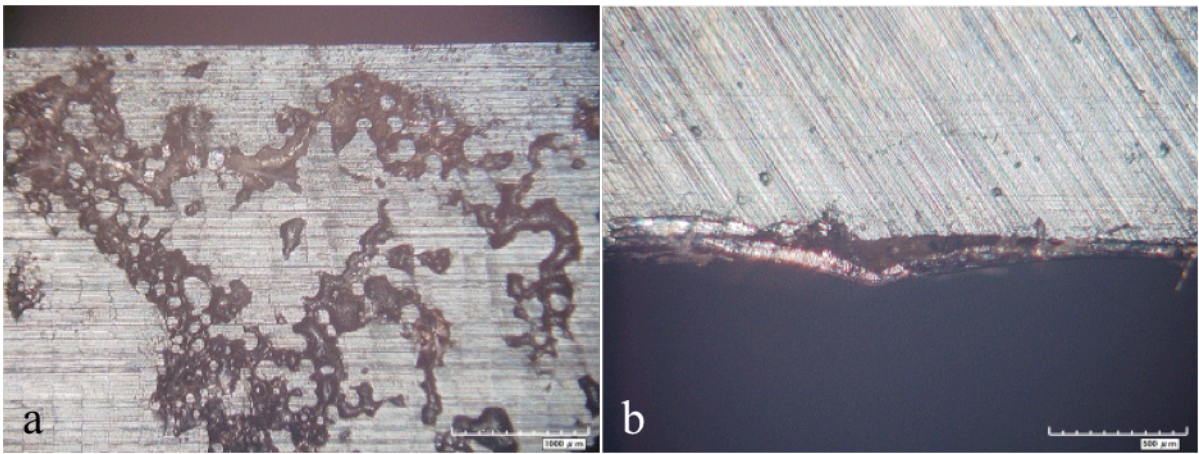


Figure 4.10. Machined tensile bar surfaces of Ti6Al4V+0.5B revealing areas containing a) voids evident by un-melted powder particles and b) layer delamination.

4.2.3. Electron Microscopy

Fracture surface analysis revealed voids on Ti6Al4V+B fracture surfaces. In some instances, un-melted powder particles were imaged within voids (Figure 4.11d). Figure 4.11c depicts the fracture surface of Ti6Al4V+1.0B. A void containing an un-melted particle was imaged directly above the initiation site of failure. Entire layers of un-melted powder near the machined edge were imaged on every Ti6Al4V+0.5B tensile sample (Figure 4.11a and b). Fracture surfaces of samples with less boron showed more plastic deformation.

Additionally, SEM analysis of polished samples revealed voids within the sample bulk (Figure 4.12).

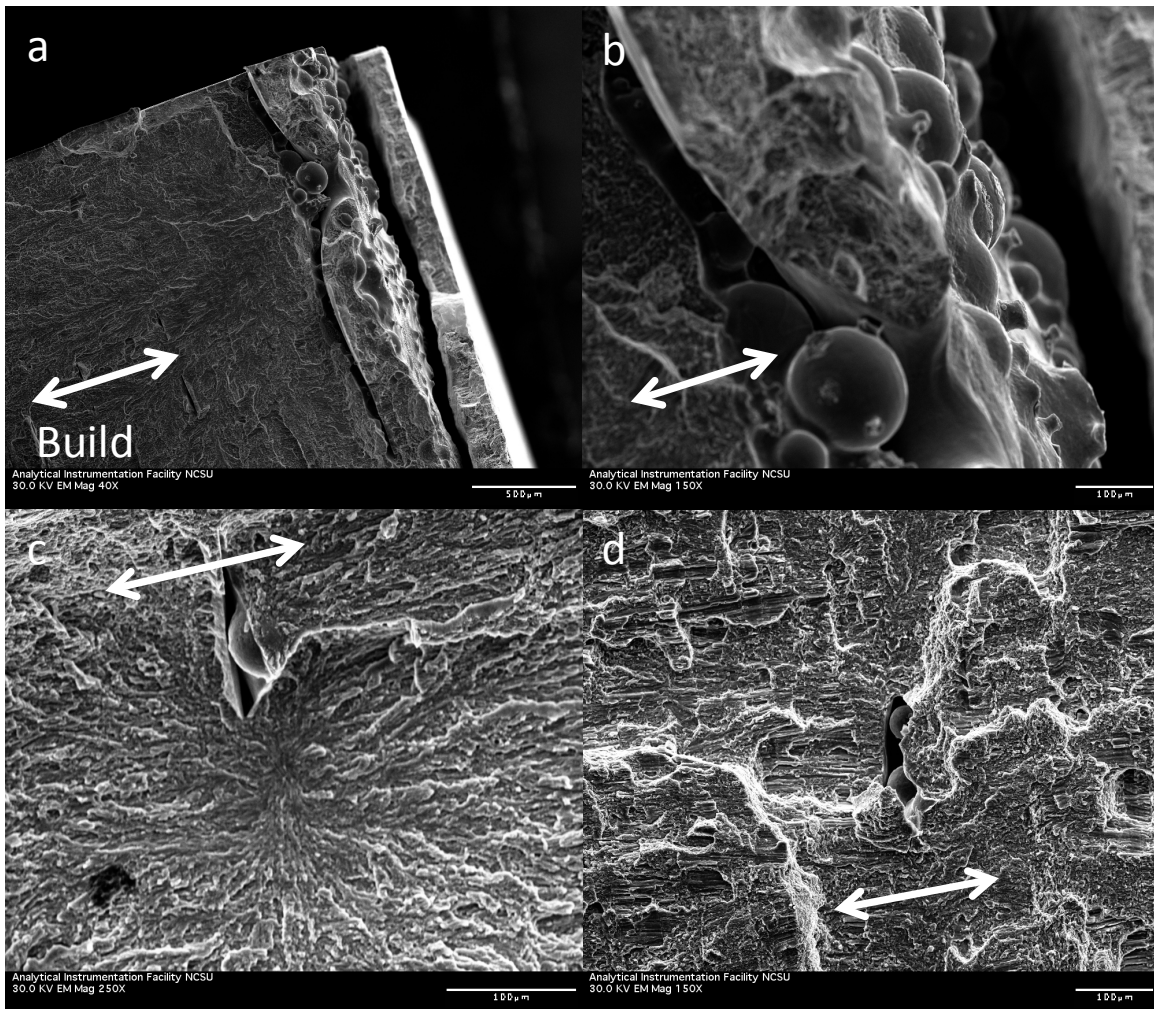


Figure 4.11. Fracture surfaces of a) and b) Ti6Al4V+0.50B, c) Ti6Al4V+1.0B and d) Ti6Al4V+0.2 showing regions of un-melted powder particles. Scale bars measure Build direction is horizontal to the page. Scale bars for a-d read 500µm, 100µm, 100µm and 100µm, respectively.

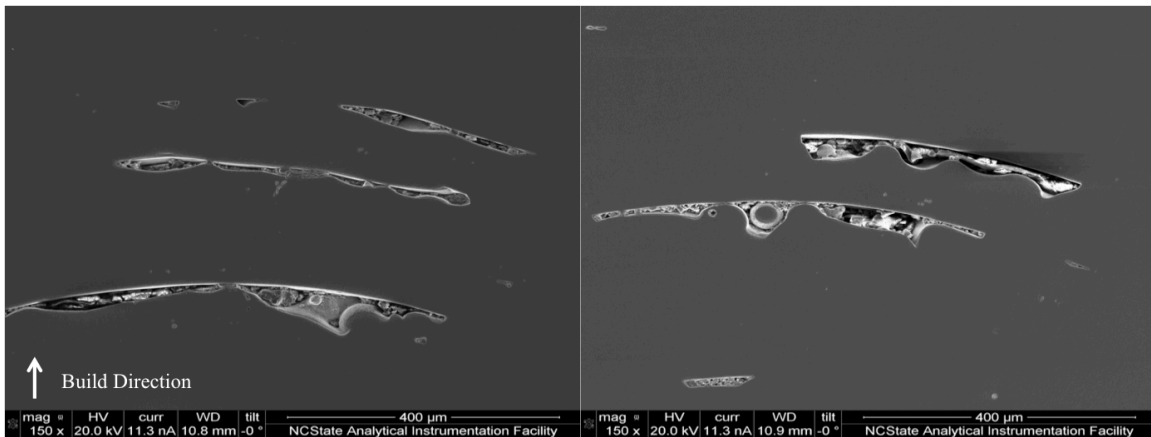


Figure 4.12. Voids in Ti6Al4V+B.

4.3. Discussion

4.3.1. Hardness

The hardness of EBM fabricated Ti6Al4V+B increases linearly with boron content. Linear trend lines fit to hardness data gave R^2 values of 0.99 and 0.90 for pre-alloyed and blended samples, respectively. Hardness is dependent on deformation mechanism because a material is plastically deformed during micro indentation testing. In literature relating to the mechanical properties of Ti6Al4V+B castings, increased hardness was attributed to the Hall-Petch and dispersion strengthening processes [Sen, 2007; Sen and Ramamurty, 2010; Zhu, 2003].

The strengthening of a material with smaller grain sizes is explained by grain boundary pinning of dislocations. Grain boundaries act as dislocation pinning points in a material. Under an applied stress, dislocations move through a grain until they reach a grain boundary

where the change in lattice orientation in adjacent grains acts as a barrier to dislocation motion. Dislocations that do not have enough energy to accommodate a change in direction will pile-up at the grain boundary. As dislocation density increases near the grain boundary, a large enough stress concentration will build up inside the grain and will reduce the energy barrier for diffusion across the grain boundary. Dislocations create a stress field around them that acts on other dislocations. Dislocation stress fields repel other dislocations, so if several dislocations are present in a pile-up the stress fields will push dislocations across the grain boundary. This leads to the initiation of slip and plastic deformation in neighboring grains and it spreads throughout the material. In smaller grains the dislocation pile-ups are proportionally smaller, so there is a smaller stress concentration to initiate slip into the next grain. This means that a larger applied stress is needed to plastically deform the material; therefore, as the grain size is reduced the strength and hardness of the material is enhanced as described by the Hall-Petch relationship in Equation 2 [Callister, 2014; Courtney, 2000].

Sen et al. demonstrated that the Hall-Petch relationship is the dominant strengthening mechanism in Ti6Al4V castings with boron additions below 0.4wt%; they fit measured yield strength and grain size to values predicted by the Hall-Petch equation [2007]. Significant grain refinement was measured for EBM Ti6Al4V+B (pre-alloyed and blended) via optical and EBSD analysis, so it is likely that the Hall-Petch mechanism has a role in hardening. As boron content increases, the strengthening effect of the Hall-Petch mechanism is neglected due to the high volume fraction of TiB [Tamirisakandala, 2003]. Zhu et al

claimed that cast Ti6Al4V+B is hardened due to dispersion strengthening of the hard TiB phase within the Ti6Al4V matrix [2003]. Similar to grain boundary strengthening, the precipitate phase acts as an obstacle for dislocation movement. In Ti6Al4V+B castings, TiB exclusively resides at the grain boundaries [Roy, 2011; Sen, 2007; Sen and Ramamurty, 2010; Tamirisakandala, 2003; Tamirisakandala, 2005; Zhu, 2003]. Dissimilarly, in Chapter 3 it was hypothesized that TiB may be dispersed homogeneously within EBM fabricated Ti6Al4V+B samples (i.e. does not collect at grain boundaries). If this prediction were correct, there would be a higher probability of TiB interacting with a dislocation in EBM Ti6Al4V+B than in cast Ti6Al4V+B. However, hardness values recorded for EBM Ti6Al4V+B were consistently lower than those reported in castings, but were within a single standard deviation [Sen, 2007]. The dispersion strengthening mechanism explains the linear increase in hardness despite the non-linear decrease in grain size.

4.3.2. Elastic Modulus

Typically, elastic modulus and hardness increase together. From Table 4.2, pre-alloyed and blended EBM Ti6Al4V+B exhibits a possible increase in elastic modulus with <1.0wt% boron content (excluding 0.50B). A more distinct increase in modulus occurs in Ti6Al4V+1B flexure bars. Enhanced modulus is expected due to the high stiffness of the TiB phase compared to the α/β matrix [Sen and Ramamurty, 2010; Zhu, 2003]. Sen and Ramamurty, reported a linear increase in elastic modulus for Ti6Al4V+B, and measured the elastic moduli of the individual α , β and TiB phases using the Oliver-Pharr method [2010].

Stiffness values of α , β and TiB phases were 132.2 ± 12.2 GPa, 81.1 ± 13.1 GPa and 384.5 ± 40.2 GPa, respectively [Sen and Ramamurty, 2010]. Elastic moduli of α and β did not vary with increasing boron addition, so mechanical improvement via solid solution strengthening is negligible in Ti6Al4V+B alloys [Sen and Ramamurty, 2010]. As boron concentration increases, there is a larger volume fraction of the stiff TiB phase and modulus is further enhanced.

4.3.3. Ductility

Percent area reduction decreases with increasing boron content in pre-alloyed and blended EBM Ti6Al4V+B. In castings, increased ductility was reported for Ti6Al4V+B when boron content was $<0.1\text{wt}\%$. Additions above $0.1\text{wt}\%$ resulted in a significant loss of ductility [Luan, 2014; Luan, 2015; Sen, 2007; Zhu, 2003].

Ductility is modified by the same mechanisms that increase strength. At low boron concentrations, grain refinement occurs due to the decrease in grain size. The Hall-Petch model is the only classic strengthening mechanism associated with enhanced ductility. Ductility enhancement per the Hall-Petch relationship is neglected as the volume fraction of TiB increases. Dispersion strengthening reduces ductility significantly. TiB precipitates are sites of crack initiation and explain the loss of tensile ductility above $0.1\text{wt}\%$ boron [Zhu, 2003].

Furthermore, during EBM fabrication, process parameters from Arcam are optimized for a specific size distribution and morphology of spherical plasma atomized Ti6Al4V. In this study, the limited quantity of powder feedstock that was produced prevented any meaningful optimization of these parameters for each different material. This may have contributed to the voids that were observed in the samples.

4.3.4. Tensile Strength

An increase in tensile strength was predicted for EBM Ti6Al4V+B due to improvements in hardness and stiffness; however, the UTS of EBM Ti6Al4V+B samples were generally below that of EBM Ti6Al4V. A decrease in tensile strength is not consistent with any literature on Ti6Al4V+B castings [Luan, 2014; Sen, 2007; Zhu, 2003].

Microscopy revealed areas of un-melted powder particles including, in one sample set, entire layers of partially melted powder (EBM Ti6Al4V+0.5B). Voids and lack of fusion between layers in EBM Ti6Al4V+B, may have contributed to premature tensile failure.

4.4. Conclusions

In this work, the effects of boron addition on the mechanical properties of EBM Ti6Al4V were analyzed. Mechanical testing was carried out on samples fabricated with EBM using pre-alloyed and blended Ti6Al4V and Ti6Al4V+B powders. Hardness increased with increasing boron content up to the 1.0 wt% boron samples used in this study, two models

have been proposed that may explain this phenomenon (1) via grain refinement, described by the Hall-Petch model, and (2) via dispersion strengthening. Further, boron addition to Ti6Al4V fabricated with EBM decreased ductility.

The data suggest that flexural elastic modulus and tensile strength of EBM fabricated samples may be improved with increasing boron additions; however, in this study, the results are inconclusive. The presence of porosity and incomplete melting of powder feedstock is believed to have contributed to the relatively high variability in the measured results.

CHAPTER 5: CONCLUSION

5.1. Summary

Ti6Al4V exhibits exceptional specific strength and good corrosion resistance; these desirable properties make Ti6Al4V the most prominently used titanium alloy accounting for more than 50% of all titanium alloy use [Leyens, 2003]. Electron beam melting is an additive manufacturing technology that focuses and directs an electron beam to selectively melt metal powder feedstock materials layer-by-layer. In addition to macro level control of complex geometries, recent work has demonstrated that for some alloy systems, it is possible to control aspects of the microstructure through controlled variations in processing parameters [Helmer, 2014; Sames, 2014]. However, for the Ti6Al4V system, the processing window of practical beam velocity and current combinations may not permit such freedom of microstructural design necessitating alternate approaches. The grain structure of Ti6Al4V produced with EBM consists of α lath structures within relatively large, columnar prior β grain boundaries, which are oriented perpendicular to the build layers. In recent literature, hypoeutectic additions of boron to Ti6Al4V have been shown to refine grain size, increase strength and reduce ductility in Ti6Al4V castings [Roy, 2011; Tamirisakandala, 2005; Zhu, 2003]. High solidification rates (10^3 - 10^5 K/s) and unique thermal histories typically found in additive manufacturing vary dramatically from those found in casting [Al-Bermani, 2010]. The objective of this study was to investigate the use of boron additions to Ti6Al4V feedstock powders in order to refine the microstructure of EBM fabricated Ti6Al4V, and to

study its effect on mechanical properties. It was hypothesized that the addition of boron, in both pre-alloyed and blended combinations, would progressively refine the columnar grain structure in EBM Ti6Al4V, improve strength and reduce ductility.

Microstructural analysis showed that the addition of boron greatly alters the microstructure of EBM fabricated Ti6Al4V. Alpha and prior β boundary sizes were reduced with boron addition. Additionally, α grains in Ti6Al4V+B did not exhibit the elongated shape typically observed in EBM or cast Ti6Al4V. The precipitation of the TiB phase was not identified using electron microscopy; however, XRD spectra show a low intensity TiB peak in the Ti6Al4V+B alloys. Furthermore, dark submicron features were observed in BSE SEM micrographs, which is consistent with observations of a TiB phase in Ti6Al4V castings reported in the literature.

In castings, β refinement was attributed to constitutional supercooling due to the negligible solid solubility of boron in Ti6Al4V. BSE images clearly show the presence of TiB at the grain boundaries in Ti6Al4V+B castings [Roy, 2011; Tamirisakandala, 2005; Zhu, 2003]. The absence of TiB at grain boundaries in EBM Ti6Al4V+B indicates that an alternate grain refinement mechanism might have taken place. It is hypothesized that the rapid solidification in EBM does not allow sufficient time for boron to diffuse to grain boundaries. In pre-alloyed samples, grains nucleate within a relatively short time domain and distinct prior β grains are not discernable in EBSD orientations maps (>0.25wt% boron).

In blended Ti6Al4V+B samples, a majority of the powder particles are Ti6Al4V, so the microstructure solidifies in a similar fashion as EBM Ti6Al4V. The microstructure is only altered when a particle containing boron is deposited and nucleation is locally enhanced.

Improvements in hardness with boron addition were measured in pre-alloyed and blended samples. Strength enhancement was attributed to microstructural refinement (Hall-Petch strengthening) and dispersion strengthening. In addition, porosity and un-melted powder particles imaged in EBM Ti6Al4V+B may have contributed to the premature failure of samples. Insufficient melting indicates that the Arcam Ti6Al4V processing parameters did not effectively melt Ti6Al4V+B powders, and should be altered. If build parameters are optimized for Ti6Al4V+B, mechanical properties should improve.

This study highlights the growing need to tailor alloy chemistry to suit the unique requirements of additive manufacturing. Preliminary work suggests that a unique grain refinement mechanism might be taking place in EBM fabricated Ti6Al4V+B, and that there is an opportunity for mechanical property improvement.

5.2. Future Work

In this work, small sample sizes were used due to limited availability of powder feedstock material. In the future it would be useful to increase sample size to validate mechanical properties, and also to expand grain size measurement. Large EBSD maps

spanning multiple millimeters would serve a significant role in measuring prior β grain boundary length and providing better representation of the EBM Ti6Al4V+B microstructure. Additionally, software packages such as ARPGE or MRL-TiBor can be used to reconstruct prior β grains in EBSD images. Roy et al. studied the effects of 0.10wt% boron additions on the crystallographic texture of Ti6Al4V+B ingots created by induction skull melting and graphite mold casting. His work demonstrated that Ti6Al4V+B showed weak and uniform texture throughout the ingot [Roy, 2011]. The reduction in α texture observable in Ti6Al4V+B was attributed to several factors including the randomization of the prior β grains, the absence of the grain boundary α phase and the nucleation of α on the TiB phase at the β grain boundaries leading to the formation of non-burgers related α grains within prior β grains [Roy, 2011]. It would be useful to use large area EBSD maps to study the development of α and β texture with boron addition.

Additionally, it is imperative to understand the microstructural evolution in EBM Ti6Al4V+B. Thermodynamic modeling software packages, such as MICRESS, will be useful in showing the effects of high cooling rates on the solidification of EBM samples and help to support theories on reasoning behind grain refinement. It is also necessary to locate the TiB phase within EBM Ti6Al4V+B samples. In one study, electron microprobe analysis (EMPA) was used to locate TiB in Ti6Al4V [Ivasishin, 2008].

There are several beam scan parameters and strategies that may be optimized to vary microstructure in EBM. Scan parameters include beam voltage, current, focus, scan rate and scan sequencing [Murr, 2015]. Adjusting build parameters, or using post-processing methods such as hot isostatic pressing can be used to produce fully dense EBM Ti6Al4V+B parts. By eliminating areas with insufficiently melted powder, tensile strength and ductility should improve. In studies on Ti6Al4V castings with <0.02wt% boron, an increase in ductility was reported. Enhancement was attributed to grain refinement (Hall-Petch) and increased grain boundary cohesion due to the presence of TiB. It would be interesting to observe the effects of <0.02wt% boron on the ductility of EBM Ti6Al4V.

REFERENCES

- Al-Bermani, S., Blackmore, M. L., Zhang, W., & Todd, I. (2010). The origin of microstructural diversity, texture, and mechanical properties in electron beam melted Ti-6Al-4V. *Metallurgical and Materials Transactions*, 41(13), 3422-3434.
- Bass, B. (2008). *Validating the Arcam EBM process as an alternative fabrication method for titanium-6Al-4V alloys (Masters Thesis)*. Retrieved from <http://www2.lib.ncsu.edu/catalog/record/NCSU2127923> (Accession No. etd-12182007-151956).
- Boyer R., Collings E.W., Welsch G. (1994). *Materials properties handbook electronic resource: Titanium alloys*. Materials Park, OH: ASM International.
- Callister, W. (2014). *Materials science and engineering: An introduction*. Hoboken, NJ: John Wiley and Sons, Inc.
- Courtney, T. H. (2000). *Mechanical behavior of materials*. Boston: McGraw Hill.
- Donachie, M. (2000). *Titanium: A technical guide*. Materials Park, OH: ASM International.
- Dunkley, J. (1998). Atomization: *metal powder production and characterization*. *Powder Metal Technologies and Applications*, 7, 35-36-52.
- Ezugwu, E. O., Wang, Z. M. (1997). Titanium alloys and their machinability-a review. *Journal of Materials Processing Technology*, 68(3), 262-274.
- Guo, N., Leu, M. (2013). Additive manufacturing: Technology, applications and research needs. *Frontiers of Mechanical Engineering*, 8(3), 215.
- Helmer, H. E., Körner, C., Singer, R. F. (2014). Additive manufacturing of nickel-based superalloy Inconel 718 by selective electron beam melting: Processing window and microstructure. *Journal of Materials Research*, 29(17), 1987-1996.
- Ivasishin, O. M., Teliovich, R. V., Ivanchenko, V. G., Tamirisakandala, S., Miracle, D. B. (2008). Processing, microstructure, texture, and tensile properties of the Ti-6Al-4V-1.55B eutectic alloy. *Metallurgical and Materials Transactions A*, 39(2), 402-416.
- Karlsson, J. (2015). *Optimization of electron beam melting for production of small components in biocompatible titanium grades (Doctoral Dissertation)*. Retrieved from Uppsala University Publications (Accession No. 978-91-554-9110-9).

- Kimmit, M. F. (1981). Laser and electron beam processing of materials. *Optics & Laser Technology*, 13(4), 222.
- Leyens, C., Peters. M. (2003). *Titanium and titanium alloys electronic resource: Fundamentals and applications*. NetLibrary. Weinheim; Chichester: Wiley-VCH.
- Luan, J. H., Jiao, Z. B., Chen, G., Liu, C. T. (2014). Improved ductility and oxidation resistance of cast Ti-6Al-4V alloys by microalloying. *Journal of Alloys and Compounds*, 602, 235-240.
- Luan, J. H., Jiao, Z. B., Heatherly, L., George, E. P., Chen, G., Liu, C. T. (2015). Effects of boron on the fracture behavior and ductility of cast Ti-6Al-4V alloys. *Scripta Materialia*, 100(0), 90-93.
- Murr, L. E. (2015). Metallurgy of additive manufacturing: Examples from electron beam melting. *Additive Manufacturing*, 5, 40-53.
- Murr, L. E., Esquivel, E. V., Quinones, S. A., Gaytan, S. M., Lopez, M. I., Martinez, E. Y., Wicker, R. B. (2009). Microstructures and mechanical properties of electron beam-rapid manufactured Ti-6Al-4V biomedical prototypes compared to wrought Ti-6Al-4V. *Materials Characterization*, 60(2), 96-105.
- Pederson, R. (2002). *Microstructure and phase transformation of Ti-6Al-4V (Masters Thesis)*. Retrieved from <http://epubl.luth.se/1402-1757/2002/30/LTU-LIC-0230-SE.pdf>
- Polmear, I. J. (1996). *Light alloys: Metallurgy of the light metals*. New York: J. Wiley & Sons.
- Roy, S., Suwas, S., Tamirisakandala, S., Miracle, D. B., Srinivasan, R. (2011). Development of solidification microstructure in boron-modified alloy Ti-6Al-4V-0.1B. *Acta Materialia*, 59(14), 5494-5510.
- Sames, W.J., Unocic, K.A., Dehoff, R.R., Lolla, T., Babu, S.S. (2014). Thermal effects on microstructural heterogeneity of Inconel 718 materials fabricated by electron beam melting. *Journal of Materials Research*, 29(17), 1920-1930.
- Schwartz A. J. (2009). *Electron backscatter diffraction in materials science*. New York: Springer.
- Sen, I., Gopinath, K., Datta, R., Ramamurty, U. (2010). Fatigue in Ti-6Al-4V-B alloys. *Acta Materialia*, 58(20), 6799-6809.

- Sen, I., Ramamurty, U. (2010). Elastic modulus of Ti–6Al–4V–xB alloys with B up to 0.55 wt.%. *Scripta Materialia*, 62(1), 37-40.
- Sen, I., Tamirisakandala, S., Miracle, D. B., Ramamurty, U. (2007). Microstructural effects on the mechanical behavior of B-modified Ti–6Al–4V alloys. *Acta Materialia*, 55(15), 4983-4993.
- Tamirisakandala, S., Bhat, R.B., McEldowney, D.J., Miracle, D.B. (2003). Affordable metal matrix composites for high performance application II proceedings. *TMS*, 28(1), 185.
- Tamirisakandala, S., Bhat, R. B., Tiley, J. S., & Miracle, D. B. (2005). Grain refinement of cast titanium alloys via trace boron addition. *Scripta Materialia*, 53(12), 1421-1426.
- Tamirisakandala, S., Miracle, D. B. (2010). Microstructure engineering of titanium alloys via small boron additions. *International Journal of Advances in Engineering Sciences and Applied Mathematics*, 2(4), 168-180.
- Wolf, R. (2005). What is ICP-MS? Retrieved from http://crustal.usgs.gov/laboratories/icpms/What_is_ICPMS.pdf
- Zhu, J., Kamiya, A., Yamada, T., Shi, W., Naganuma, K. (2003). Influence of boron addition on microstructure and mechanical properties of dental cast titanium alloys. *Materials Science and Engineering: A*, 339(1–2), 53-62.

APPENDIX

Appendix

Peak lists for Ti and TiB are reported in Tables A.1 and A.2, respectively.

Table A.1. Peak list for titanium. Reference code 00-001-1197.

| 2Theta (deg) | Intensity (%) |
|---------------------|----------------------|
| 35.023 | 40 |
| 38.439 | 40 |
| 40.227 | 100 |
| 52.88 | 40 |
| 62.728 | 40 |
| 70.178 | 50 |
| 76.084 | 40 |
| 77.549 | 30 |
| 81.506 | 10 |
| 85.95 | 10 |

Table A.2. Peak list for TiB. Reference code 00-006-0641.

| 2Theta (deg) | Intensity (%) |
|---------------------|----------------------|
| 36.65 | 80 |
| 42.612 | 100 |
| 61.799 | 60 |
| 73.997 | 40 |
| 77.926 | 30 |
| 93.221 | 20 |